PROBING WEAKLY BOUND LONG-RANGE RYDBERG MOLECULES BY QUANTUM BEATING EXPERIMENTS IN RUBIDIUM VAPOR

BY

RUI SU

DISSERTATION

Submitted in partial fulfillment of the requirements
for the degree of Doctor of Philosophy in Electrical and Computer Engineering
in the Graduate College of the
University of Illinois at Urbana-Champaign, 2020

Urbana, Illinois

Doctoral Committee:

Professor J. Gary Eden, Chair
Professor Viktor Gruev
Associate Professor Virginia Lorenz
Assistant Professor Kejie Fang
Assistant Professor Joshua Vura-Weis

ABSTRACT

Weakly bound long-range Rydberg molecules (LRRM) associated with rubidium atomic states with low angular momentum and very low principal quantum numbers ($7s$, $8s$, $5d$, $6d$) are observed in a quantum beating experiment for the first time. The experiments are conducted using parametric four-wave mixing (PFWM) in a pump-probe fashion. Fourier analysis of the time-domain data yields a spectrum on which various quantum beats are identified. Energy spacings between adjacent vibrational levels within each LRRM's quantum well manifest on the spectrum as overtones on both sides of the $7s$-$5d_{5/2}$ and $8s$-$6d_{5/2}$ atomic quantum beats at 18.225 THz and 10.726 THz, respectively. From the observed vibrational term energy spacings, we are able to extract vibrational constants for three potential wells and calculate their dissociation energies and potential energy curves using Morse potential. Despite the fact that there are no direct results published in the literature associated with s and d states at our principal quantum numbers, we are able to validate our observations by comparing our vibrational constants with those of the p state and our dissociation energies with those extrapolated from higher principal quantum numbers. The comparison shows excellent agreement with existing studies. The study demonstrates a new experimental technique to study LRRM that does not involve Bose-Einstein condensates and yet can resolve vibrational levels within quantum wells of several cm^{-1} deep. The technique is also versatile in studying heteronuclear and polyatomic LRRM.

To my mother, Dongmei

ACKNOWLEDGMENTS

It is a scientist's simple intention, but also the ultimate satisfaction, to contribute new things to the knowledge of the human race. It is an honor and a privilege to contribute my own. This endeavor is not possible without the help and support from many people I want to give thanks to.

First and foremost I would like to thank my advisor, Prof. J. Gary Eden for his support, guidance, vision and insight; for his knowledge, experience and the generosity in sharing them without reservation; and for his inspiring belief in science, creativity and the intrinsic value of such pursuits. Throughout the years in graduate school, I have learned from him as many things as the cups of coffee he bought for his students, uncountable. They will continue to inspire me long after I graduate.

I am thankful for LOPE, a lab where bold ideas can get heard and implemented, where we both challenge and collaborate with each other to make a real difference, and where our friendships have given me a lot of fun memories. Thank you Tom Houlahan, Tom Galvin, Zhen Dai, Kyle Raymond, Andrey Mironov, William Goldshlag, Jose Rivera, Wenting Chen, Charles Shin, Oluwayemisi Sonoiki, Sehyun Park, Yin Huang, Hee Jun Yang, Peter Peng Sun, Austin Steinforth, Jinhong Kim, Kavita Desai, Wenyuan Chen, Mustafa Sak, Christi Coxsey and Prof. Sung-Jin Park.

This dissertation is not possible without "generations" of my predecessors at LOPE who devoted their graduate study to the work on quantum beating experiments. In particular, I want to give thanks to William Goldshlag whose outstanding work laid a robust foundation that my work was built on. He is also a good teacher who generously helped me on my research and a friend who I often look up to.

I want to say thank you to my family, especially my parents and grandparents in China. Thank you for your unwavering love, for always believing in me, and for enduring such a long period of physical separation from me. I

want to give my special thanks to my mother, Dongmei, to whom I dedicate this work. Her love and support, and her spirit of hope, kindness, courage and perseverance, inspire me in both her words and action.

This dissertation was accomplished during the global COVID-19 pandemic, at a time when the value of scientific knowledge has never been felt so strongly. It reminds us of the great privilege and responsibility of being a scientist and engineer. May our work benefit the future of humanity.

TABLE OF CONTENTS

CHAPTER 1

INTRODUCTION

This dissertation introduces a new experimental technique to study long-range Rydberg molecules (LRRMs), through quantum beating spectroscopy. By analyzing the quantum beating spectrum, we are able to observe vibrational structures inside shallow potential wells of long-range Rb_2 photoassociated in heated rubidium gas vapor. We are able to extract vibrational constants and binding energies of these long-range potential wells, whose values are found to be close to those extrapolated from published data. Our observations of the long-range Rb_2 focus on those whose Rydberg electrons are of low angular momentum quantum numbers ($l = 0, 2$) and very low principal quantum numbers ($n = 5 - 8$), which are not well studied in existing literature. Produced in heated gas vapor (mostly 170 °C), the long-range Rb_2 have dissociation energies of less than 10 cm^{-1}, which are two orders of magnitude smaller than the thermal energy. Quantum beating spectroscopy is employed in the study of LRRMs for the first time, leveraging the short duration and large bandwidth of femtosecond lasers, in contrast to the more commonly used methods that involve precision scanning of narrow-bandwidth lasers in combination with field ionization and Bose-Einstein condensates (BEC). Our method also makes it easier to study the heteronuclear LRRM, such as Rb^*-rare gas molecules, which can be challenging to study in ion traps.

Long-range Rydberg molecules, or LRRMs, are a class of molecules whose internuclear distances can span from tens of Bohr radii to several thousand Bohr radii, much larger than the traditionally studied short-range molecules whose internuclear distances typically range from several to, at maximum, a few tens of Bohr radii. The chemical bond of the LRRM is formed as a result of highly excited Rydberg electron being scattered by another atom that is far away, which is fundamentally different from the covalent or ionic bonding mechanism of common short-range molecules. Our research looks at the LRRM formed from Rydberg atoms with very low principal quantum

numbers, which is particularly challenging because the Rydberg electron is closer to other inner-well electrons.

This chapter first introduces the theoretical background to understand LRRM. This introduction includes three parts; first, using quantum defect theory to understand the energy structure of a Rydberg atom; second, using partial wave decomposition to understand the electron-atom scattering process, which is the bonding mechanism to form LRRM; and third, using the Fermi pseudopotential to derive the Born-Oppenheimer potential energy curve (PEC) of such LRRMs. Accompanying the PECs are vibrational energy levels that can be found in each potential well.

Next, I will introduce the working principles of the quantum beating phenomenon, which is employed as an experimental technique to study LRRMs for the first time.

1.1 Long-range Rydberg Molecule (LRRM)

Long-range Rydberg molecules (LRRMs) were first predicted in theory by Greene *et al.* [1] in 2000. The idea is that if a highly excited Rydberg electron far away from the ionic core gets scattered by another atom at ground state, the interaction enables a weak force of attraction between the two atoms, causing small ripples in the PEC at long internuclear distances, essentially forming a "molecule". Since the fundamental mechanism of forming the molecule at long range is the interaction between a low kinetic energy Rydberg electron and a neutral particle, the theory to describe this type of interaction was already studied decades ago. Of particular importance is the work of Fermi, who argued that since the de Broglie wavelength of the highly excited Rydberg electron is much greater than the extent of the neutral atom's polarization potential, the interaction should only cause a scattering phase shift to the Rydberg wave function [2]. The interaction can then be described with the concepts of scattering length and pseudopotential. Omont [3] later extended this theory by making the scattering length energy-dependent and incorporating other factors. Greene *et al.* [1] predicted this type of interaction should form a new type of molecule at long range, and pointed out the Born-Oppenheimer PEC of such molecules can be derived from Fermi's pseudopotential. The wavefunctions of these predicted LRRMs

are also unique in the sense that their electronic wave functions may resemble the shape of a trilobite fossil, and thus are also called "trilobite states". In 2002, another type of LRRM, whose electronic wave function resembles the shape of a butterfly, was theoretically predicted. These states are usually referred to as "butterfly states" [4, 5].

Experimental observation of these LRRMs took a slower path. In 2006, Greene *et al.* found that the potential minima of such predicted PECs agree well with the positions of the satellite peaks on the spectra of line-broadening experiments in rubidium vapor, providing initial experimental evidence for the existence of LRRM [6]. Similar experimental verification using line-broadening experiments was conducted by Vadla *et al.*, which extends the species to homonuclear and heteronuclear diatomic molecules formed by potassium, rubidium and cesium [7]. None of these experiments, however, provides enough resolution to verify the vibrational structures inside the predicted potential well. This was changed with the introduction of Bose-Einstein condensates (BECs), whose low temperature prevents the weak chemical bond from being destroyed by thermal motions. Higher resolution experimental work started to emerge on a larger scale. In 2009, almost a decade after LRRM was proposed by Greene *et al.*, Bendkowsky *et al.* [8] reported the first observation of the LRRM's vibrational spectra in rubidium associated with the Rydberg electron's principal quantum number n of 34-40 and angular momentum quantum number l of 0. A plethora of experimental measurements of LRRM vibrational structures were conducted on LRRMs of various atoms at different quantum numbers, with or without fine structure or hyperfine structure, with different isotopes, etc. (see [9–15] for a few examples). The agreement between experimental results and theory proves the existence of LRRM and shows the extent to which current theoretical models can apply.

Bose-Einstein condensates, though helpful to the observation of LRRM, are not the necessary condition for either the formation or observation of LRRM. LRRMs exist, when Rydberg electrons are present, given proper excitations, even at high temperature. In fact, [6] and [7] reported the observation of potential energy minima of Rb_2 LRRM for rubidium vapors in a heat pipe, through absorption spectroscopy. The experiments suffer from low resolution, as can be predicted for attempting to observe LRRM without cooling and using Doppler-limited spectroscopic method. In our work, however, we are

able to observe LRRM in heated rubidium vapor with resolved vibrational structure by using femtosecond laser source in combination with quantum beating spectroscopy. This unique combination eases LRRM observation without BEC in two ways. First, quantum beating spectroscopy is a Doppler-free technique [16]. Second, the femtosecond laser in conjunction with pump-probe technique essentially freezes the system in time for data scan. These unique benefits make observing LRRM without BEC possible.

In this dissertation we focus on the diatomic LRRM formed in rubidium. Of particular interest are the PECs of LRRM, from which vibrational spectrum can be derived. We thus provide some background in this chapter on how the PECs of LRRM can be derived from first principles in quantum mechanics. This process can not only help us understand the formation mechanism of LRRMs and introduce the special features of LRRM, but also provide the theoretical background for understanding the vibrational spectroscopic observations we are going to present in Chapter 3. Other theoretical aspects of LRRM can be found in review papers such as [17–19].

Our discussion on deriving LRRM PEC follows a "theoretical framework" shown in Figure 1.1. In short, the quantum defect theory describes the atomic energy levels of Rydberg atoms, while the electron-atom scattering phase shifts describe the interaction between an excited Rydberg electron and a neural atom. Finally, the Fermi pseudopotential unites the two to compute the PEC. We shall now discuss them in detail.

1.1.1 Rydberg Atom and Quantum Defect Theory

The formation of LRRM relies on a Rydberg electron, an excited electron whose wave function extends over a large range beyond the ionic core and exhibits large de Broglie wavelength. An atom with such an electron is called a Rydberg atom, and can be described by quantum defect theory.

For simplicity, we focus on alkali atoms, the Rydberg atoms that have only one Rydberg electron in the outermost shell (valence electron). When the Rydberg electron is excited to a state with high principal quantum number [20], its wave function extends far away from the nucleus and the rest of the electrons. From the perspective of the Rydberg electron, the ensemble of the nucleus and other electrons looks like a single entity, an ionic core.

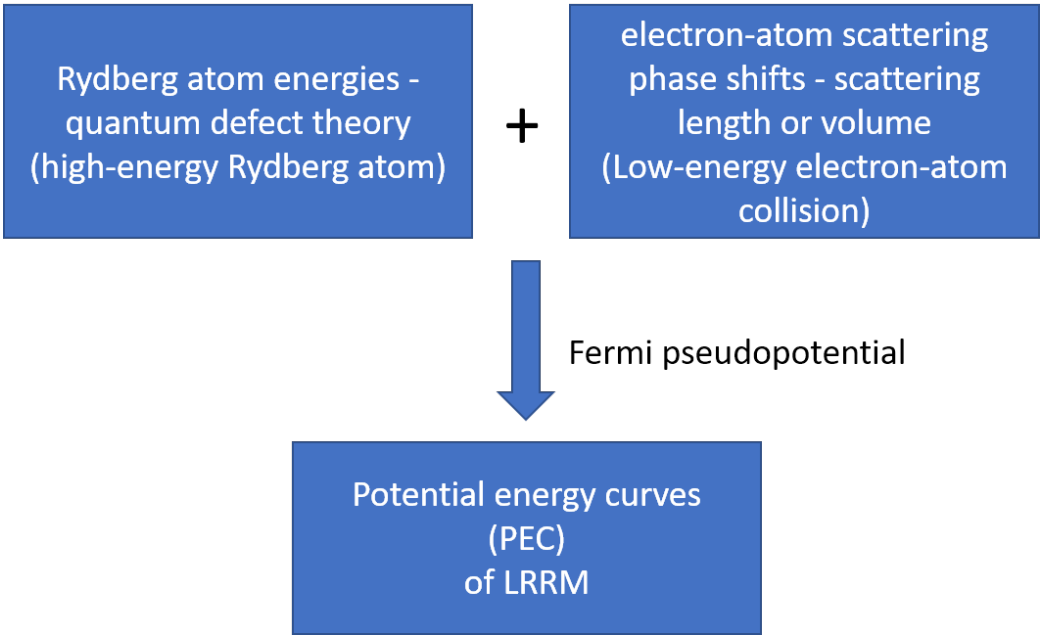

Figure 1.1: The theoretical framework for deriving the potential energy curves (PEC) of long-range Rydberg molecules (LRRMs). The Fermi pseudopotential unites the quantum defect theory and the low-energy electron-atom scattering phase shifts to produce LRRM PEC.

.

The system thus resembles that of an hydrogen atom. This simplifies the description of the Rydberg atom by using a modified hydrogen model and the deviation from a real hydrogen atom can be described by a quantum defect.

For a hydrogen atom, all energy levels can be described by the following equation [21, 22]:

$$E'_n = -hc\frac{R_H}{n^2} = -13.6 \text{ eV} \cdot \frac{1}{n^2} \tag{1.1}$$

where n is the principal quantum number, h the Planck's constant, c the speed of light and R_H the Rydberg constant for hydrogen which is given by [13]

$$R_H = R_\infty \frac{M_p}{m_e + M_p} \approx R_\infty = \frac{e^4 m_e}{8c\epsilon_0^2 h^3} = 10979731 \text{ m}^{-1} \tag{1.2}$$

where R_∞ is the Rydberg constant [23], M_p the proton mass, m_e the electron mass, e the electron charge and ϵ_0 the vacuum permittivity.

For Rydberg atoms, Equation 1.1 can be modified by replacing the principal quantum number n with an effective quantum number $n^* = n - \delta_{nlj}$. All

energy levels in a Rydberg atom other than hydrogen can then be written as follows:

$$E_n = -hc\frac{R_\infty}{n^{*2}} = -hc\frac{R_\infty}{(n-\delta_{nlj})^2} \tag{1.3}$$

where δ_{nlj} is the quantum defect, which is a function of the principal quantum number n, electron angular momentum quantum number l and total angular momentum quantum number j.

Because the core of the Rydberg atom is composed of not only protons but also inner shell electrons, at low principal quantum numbers the Rydberg electron is closer to these inner shell electrons and thus their interactions become stronger. The Rydberg atom becomes less "hydrogen-like". As a result, the quantum defect δ_{nlj} is dependent on the principal quantum number n. This dependence can be easily seen from the Rydberg-Ritz formula [24]

$$\delta_{nlj} = \delta_0 + \frac{\delta_2}{(n-\delta_0)^2} + \frac{\delta_4}{(n-\delta_0)^4} + ... \tag{1.4}$$

where the higher order terms get increasingly smaller.

Additionally, a more realistic treatment of the quantum defects takes into account the spin-orbit coupling and relativistic effect [25]. As a result, δ_0, δ_2,... in Equation 1.4 become dependent on both quantum number l and j. A list of quantum defect parameters δ_0 and δ_2 for rubidium at low-l levels can be found in Table 1.1. Following a similar trend of quantum defect dependence on n, as l gets bigger, the Rydberg electron is found farther away from the core so the defect becomes smaller and the Rydberg atom becomes more hydrogenic, as reflected in Table 1.1.

Table 1.1: Quantum defect parameters (used in Equation 1.3 and 1.4) δ_0 and δ_2 for rubidium in atomic units. The data were taken from [26, 27].

Rb	δ_0	δ_2
$s_{1/2}$	3.131 1804	0.1784
$p_{1/2}$	2.654 8849	0.2900
$p_{3/2}$	2.641 6737	0.2950
$d_{3/2}$	1.348 091 71	-0.602 86
$d_{5/2}$	1.346 465 72	-0.596 00
$f_{5/2}$	0.016 5192	-0.085
$f_{7/2}$	0.016 5437	-0.086

1.1.2 Electron-Atom Scattering and Fermi Pseudopotential

Because a highly excited Rydberg electron's de Broglie wavelength is much larger than the extension of a ground state atom's polarization potential, the scattering process of the Rydberg electron from the ground state atom can be seen as only exerting phase shifts to the Rydberg atom's wave function [2]. This process then can be decomposed into phase shifts of partial waves, in particular, phase shifts of the s and p waves.

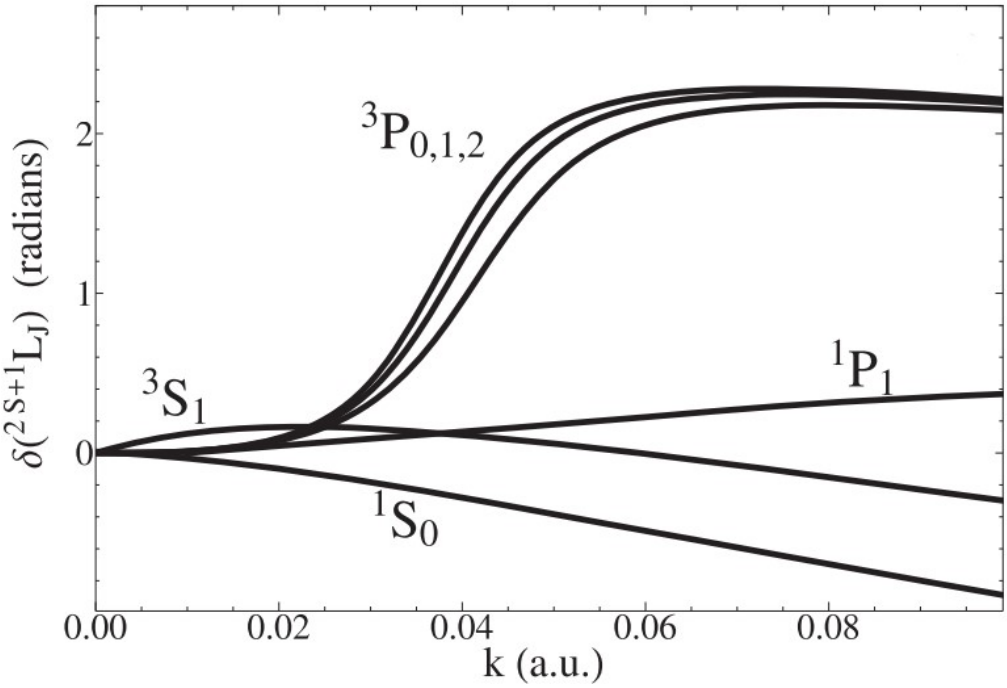

Figure 1.2: Rubidium scattering phase shifts δ as a function of electron wave number k. Terms are labeled as $^{2S+1}L_J$ where $J = L + S$. Reprinted with permission from [28]. Copyright by the American Physical Society.

Figure 1.2 shows the s and p-wave scattering phase shifts δ_s and δ_p (in radians) for rubidium as a function of electron wave number k. The wave number k is defined by the kinetic energy of the Rydberg electron and is related to the electron energy through

$$\frac{1}{2}k^2(R) = \varepsilon + \frac{1}{R} \tag{1.5}$$

where R is the internuclear distance and ε is the Rydberg electron energy defined in atomic units $\varepsilon = -1/2n^2$. Another form of ε in SI units is the familiar Equation 1.3 with the quantum defect embedded in n.

Phase shifts in turn define the s-wave scattering length $a_s(k)$ and p-wave scattering volume $a_p^3(k)$ as follows:

$$a_s[k(R)] = (-\frac{\tan\delta_s[k(R)]}{k(R)}) \tag{1.6}$$

$$a_p^3[k(R)] = (-\frac{\tan\delta_p[k(R)]}{[k(R)]^3}) \tag{1.7}$$

According to the definition, we see that the magnitudes of scattering length and scattering volume are functions of the Rydberg electron's kinetic energy, which is ultimately a function of the internuclear distance R. In fact, k, δ_s, δ_p, $a_s(k)$ and $a_p^3(k)$ are all functions of R.

The scattering length and scattering volume are defined to characterize the role of Rydberg electron scattering phase shifts in determining the LRRM electronic potential. As illustrated in Figure 1.1, Fermi's pseudopotential links the above-mentioned quantum defect theory and electron-atom scattering phase shifts to generate the LRRM's PEC, in the following way.

The total Hamiltonian of the LRRM H is composed of the Hamiltonian of the unperturbed Rydberg electron H_0 and an perturbing term, the Fermi pseudopotential V_{fermi}

$$H = H_0 + V_{\text{fermi}}(\overrightarrow{R}, \overrightarrow{r}) \tag{1.8}$$

where $\overrightarrow{R}$ is the position vector from the Rydberg core to the ground-state atom (perturber) and $\overrightarrow{r}$ is the position vector from the Rydberg core to the Rydberg electron. The Fermi pseudopotential V_{fermi} is related to the electron-atom scattering phase shifts δ_l through its definition generalized by Omont [3]

$$V_{\text{fermi}}(\overrightarrow{R}, \overrightarrow{r}) = 2\pi \sum_{l=0}^{\infty}(2l+1)\delta^3(\overrightarrow{r} - \overrightarrow{R}) \times (-\frac{\tan\delta_l[k(R)]}{k(R)})P_l(\frac{\overleftarrow{\nabla} \cdot \overrightarrow{\nabla}}{[k(R)]^2}) \tag{1.9}$$

The eigenvalues of H_0 are the unperturbed energies of an Rydberg atom E_{nl} (Equation 1.3). Perturbation theory can then be used to derive the PEC of LRRM, which is the total energy $E = E_{nl} + E_{\text{perturb}}$. For a diatomic molecule and considering only s and p-wave pseudopotentials, PECs only have Σ and Π symmetries. At low angular momentum quantum number

(usually $l \leqslant 2$), non-degenerate perturbation theory is used to derive the E_{perturb} [19], given by

$$E^{\Sigma}_{low\,l}(R) = 2\pi(\frac{2l+1}{4\pi})(a_s[k(R)][\frac{u_{nl}(R)}{R}]^2 + 3a_p^3[k(R)]|\frac{du_{nl}(R)/R}{dR}|^2) \quad (1.10)$$

$$E^{\Pi}_{low\,l}(R) = 6\pi a_p^3[k(R)](\frac{(2l+1)(l+1)l}{8\pi})[\frac{u_{nl}(R)}{R^2}]^2 \quad (1.11)$$

where u_{nl} denotes the unperturbed radial wave function of the Rydberg electron. We see that Equations 1.10 and 1.11 are basically composed of the products between the scattering length (or volume for p-wave) and the square of the unperturbed radial wave function (or its gradient for p-wave). This implies the LRRM's PEC oscillates as a function of the internuclear distance R in a similar manner to the unperturbed Rydberg electron's radial wave function. As a result, LRRM's PEC may contain multiple electronic wells that support different series of vibrational energy levels.

Equations 1.10 and 1.11 are derived for the case where the Rydberg electron involved in forming the LRRM possesses only low angular momentum ($l \leqslant 2$, i.e. s, p and d states). For Rydberg electrons of higher angular momentum quantum number l, degenerate perturbation theory has to be used. The high degeneracy of the states yields exotic shapes for the molecules' wave functions that are distinctive to LRRM, i.e. shapes that resemble a trilobite fossil or butterfly (see insets of Figure 1.3 and also Figure 1.5, 3D visualizations of the LRRM's wave functions at different viewing angles). From the visualization of their wave functions we see a high localization of the probability density near the ground state atom perturber, a special property of these trilobite and butterfly states. Because the wave functions exhibit apparent asymmetry to the plane perpendicular to the line joining two atoms, these molecules possess non-zero electric dipole moments, in spite of being homonuclear diatomic molecules, making them sensitive to external control and manipulation.

Figure 1.3 [19] shows a panoramic view of the theoretically derived PECs for both low l and high l of long-range Rb_2, between $n = 29$ and $n = 30$ manifolds. Figure 1.4 zooms in on the details of certain regions in Figure 1.3. The wells of the low-l PECs asymptotically associated with the $33s$, $32p$ and $31d$ states can only be seen on Figure 1.4 but are too shallow to be spotted on Figure 1.3, where the much deeper wells of trilobite and butterfly states

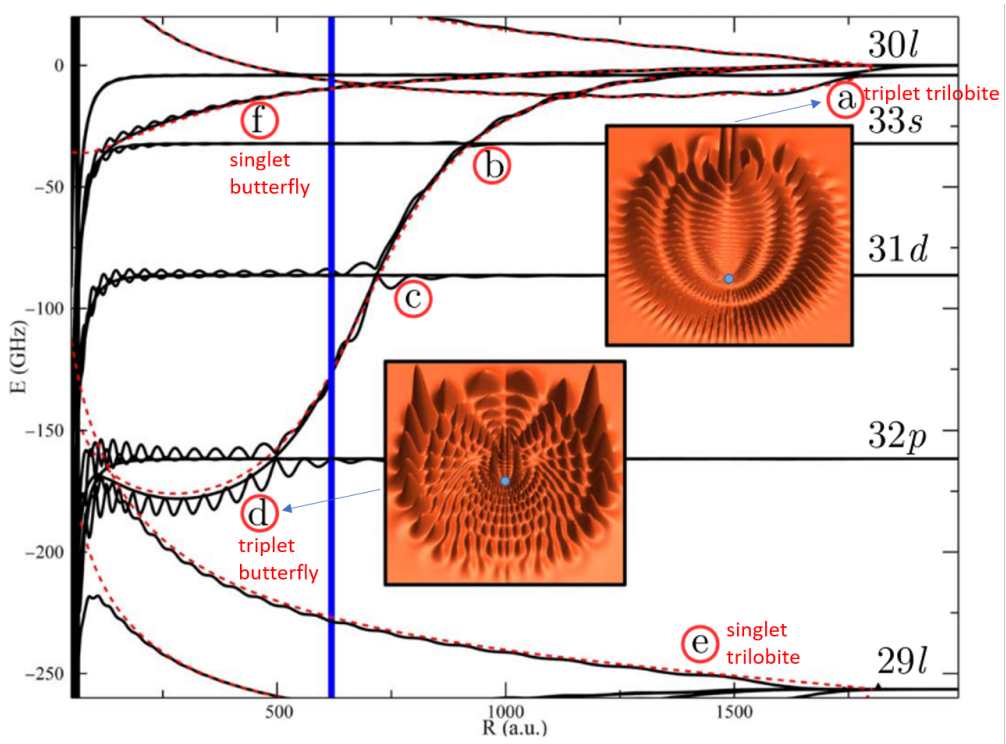

Figure 1.3: Panoramic view of the theoretically predicted long-range Rb_2 PEC, between $n = 29$ and $n = 30$ manifolds. Solid black curves are computed from Fermi pseudopotential and dashed red curves are computed using an alternative method [19]. The blue vertical line marks the location of p-wave shape resonance. (a) The triplet trilobite PEC and its wavefunction are plotted in cylindrical coordinates. (b) PEC associated with Rb $33s$ state and its intersection with the triplet butterfly PEC. (c) PEC associated with Rb $31d$ state and its intersection with the triplet butterfly PEC. (d) The bottom of the triplet butterfly PEC and its wavefunction plotted in cylindrical coordinates. (e) The singlet trilobite PEC. (f) The singlet butterfly PEC. Reprinted with permission from [19]. Copyright by IOP Publishing. All rights reserved.

are easily identifiable. Let us discuss each feature in Figure 1.3 and 1.4:

(a) The high-l triplet trilobite PEC has an overall wide well spanning several hundred Bohr radii with a depth of ≈12 GHz. The well is both wider and deeper compared to the sub-GHz-deep wells associated with the low l atomic state, e.g. $33s$ shown in Figure 1.4 (c). The trilobite-shaped wave function density is plotted next to the PEC. A zoom-in view of the area is shown in Figure 1.4 (a) where oscillations at the bottom of this triplet trilobite well can be seen.

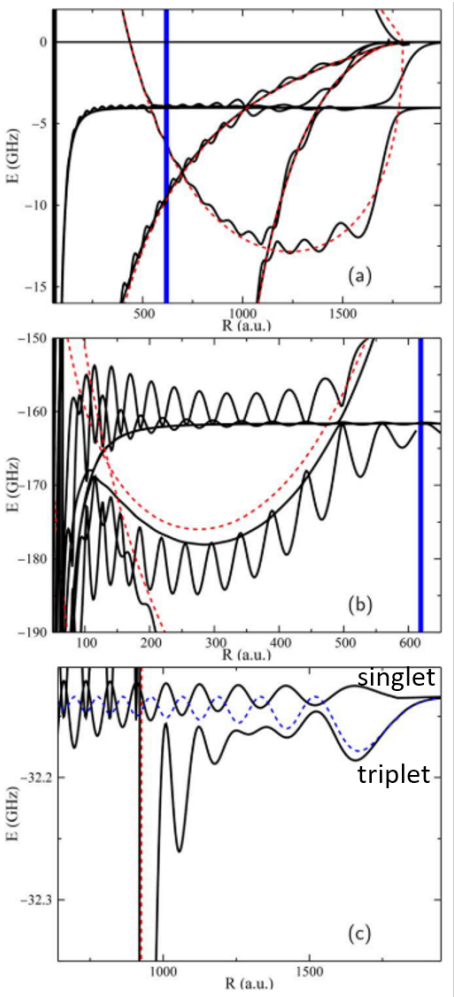

Figure 1.4: Zoom-in view of certain areas of the long-range Rb_2 PEC in Figure 1.3. (a) Near the bottom of the triplet trilobite potential well. (b) Near the bottom of the triplet butterfly potential wells. (c) The singlet and triplet $33s$ potential curves. The dashed blue curve in (c) designates a triplet PEC without taking into account of the p-wave potential. The vertical blue lines mark the location of p-wave resonance. Reprinted with permission from [19]. Copyright by IOP Publishing. All rights reserved.

(b) PEC associated with Rb $33s$ state and its intersection with the triplet butterfly PEC. The depth of the well and the oscillation of PEC can only been seen in the zoom-in view shown in Figure 1.4 (c). Figure 1.4 reveals the singlet and triplet components. Both the singlet and triplet curves exhibit oscillatory behavior and the triplet potential is deeper than the singlet. The deepest well is the outermost well of the triplet potential, although all these wells are pretty shallow, only a few tens

of MHz deep.

(c) PEC associated with Rb $31d$ state and its intersection with the triplet butterfly PEC. It behaves similarly to (b), the $33s$ potential.

(d) The triplet butterfly potential dives down through the triplet trilobite potential and the $33s$, $31d$, $32p$ potential. Its bottom is close to the $32p$ potential. The wave function density plot is also shown. The zoom-in view of this PEC is shown in Figure 1.4 (b) which reveals oscillatory wells at the bottom.

(e) The singlet trilobite PEC shows a monotonic trend.

(f) The singlet butterfly PEC shows a monotonic trend.

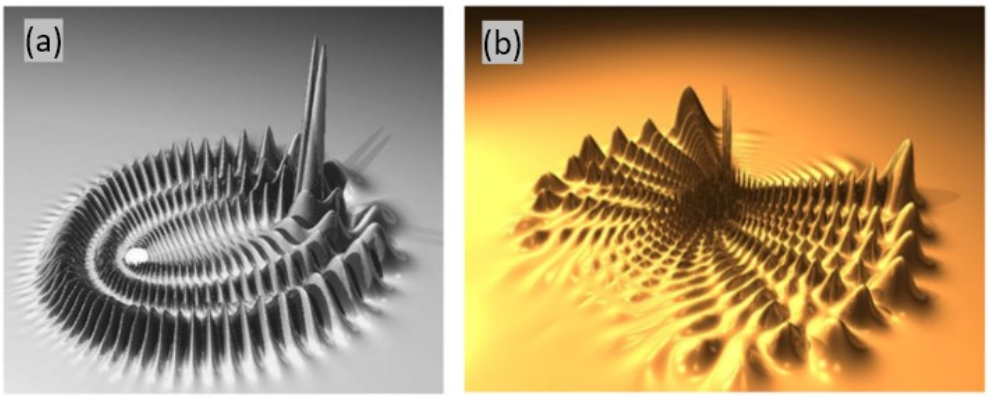

Figure 1.5: Cylindrical coordinate surface plot of the electronic probability density for high-l class LRRMs. (a) Trilobite states. Reprinted with permission from [1]. Copyright by the American Physical Society. (b) Butterfly states. Reprinted with permission from [4]. Copyright by IOP Publishing. All rights reserved.

We must note that in our experiment our observation of the LRRM molecular structure is associated with the $5d$ - $8s$ states of the rubidium atom (specifically, $5d$, $6d$, $7s$ and $8s$). The principal quantum numbers are almost one order of magnitude smaller than those shown in Figure 1.3 and 1.4. In theory, their PECs should follow a similar trend governed by the scaling law, i.e. the depths of the potential wells associated with the low-l states scale as n^{-6} while the trilobite potential wells scale as n^{-3}, with the trilobite and butterfly potential wells significantly deeper than those associated with

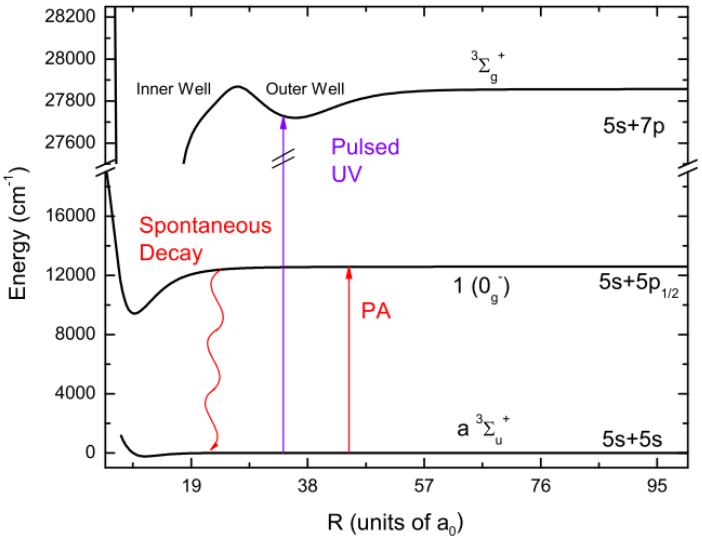

Figure 1.6: Carollos *et al.*'s experimental procedure to produce long-range Rb_2. Ground state atoms are first photoassociated (PA) to a high vibrational level ($v' \approx 173$) of the $1(0_g^-)$ state below the $5p_{1/2}$ asymptote, which spontaneously decay to the upper levels ($v" = 35, 36$) of the $a^3\Sigma_u^+$ state. The molecules are then excited to the long-range $^3\Sigma_g^+$state of $Rb_2(7P + 5S_{1/2})$ with pulsed UV light. Reprinted with permission from [29]. Copyright by the American Physical Society.

low-l states. Nonetheless, the method of Fermi pseudopotential relies on the assumption that the Rydberg electron is highly excited (far away from the ionic core) and with low-kinetic energy (low-energy electron-atom scattering). At low principal quantum numbers these assumptions start to break down so these theories cannot predict the PECs as accurately as those of the high principal quantum numbers. Thus at low principal quantum numbers, both the traditional covalent bonding mechanism and the Rydberg electron-atom scattering mechanism are involved in the formation of Rb long-range molecules. As a result, there has not been a theoretical model to accurately describe LRRM at low principal quantum numbers, nor are there enough experimental investigations. For rubidium, for example, the lowest n for (nS + $5S_{1/2}$) LRRM that has been experimentally verified is $n = 34$ [8], where only two vibrational levels of the outermost well are verified with theory. For (nD + $5S_{1/2}$) LRRM, the lowest n that has been experimentally studied is $n = 24$ [30], where differences between isotopes and spin couplings were resolved, but again limited to only two vibrational energy levels in the outer

region of the PEC. For (nP + $5S_{1/2}$) LRRM, however, significant lower n was achieved in experiments, due to their easier production with single color laser excitation. Minima of multiple wells on the same PEC of Rb_2(7P + $5S_{1/2}$) were roughly matched to the line-broadening spectra obtained from high-temperature rubidium in a heat pipe [6]. Bellos *et al.* obtained vibrational spectra of Rb_2(7, 9-12P + $5S_{1/2}$) through bound-bound excitation [11]. Carollo *et al.*'s experiments resolved several vibrational structures in Rb_2(5P + $5S_{1/2}$) and improved the resolution of the vibrational spectra of Rb_2(7P + $5S_{1/2}$) [29]. Bellos and Carollo's procedure of producing Rb_2(nP + $5S_{1/2}$) is shown in Figure 1.6. Among the long-range Rydberg Rb_2 of low principal quantum numbers and low angular momentum l, Rb_2(nP + $5S_{1/2}$) has the lowest achieved principal quantum numbers whose vibrational structure has been resolved in experiments so far ($n = 5$). However, neither Bellos nor Carollo were able to give definite vibrational quantum number assignments to the vibrational structures on their spectra.

In conclusion, rubidium LRRMs at low principal quantum numbers, especially s and d states with n smaller than 10, have not been not well studied, making our study particularly meaningful. Our discussion so far provides us with the essential background in the forming mechanism of LRRM to understand our experiments. Now we need to introduce the principles of the experimental technique that enables us to observe the rubidium LRRM at such low principal quantum numbers, i.e. the quantum beating spectroscopy.

1.2 Quantum Beating and Pump-Probe Experiment

This dissertation introduces a new experimental technique to study LRRM, through quantum beating spectroscopy, whose theoretical background is provided in this section. First we introduce the concept of wave packets in quantum physics and the quantum beating phenomenon. The quantum beating phenomenon and the parametric four-wave mixing (PFWM) process are applied in a pump-probe experiment to observe the molecular structure of LRRM.

1.2.1 Quantum Beating Phenomena

In quantum mechanics, a wave packet is a time-dependent superposition of the wave functions of stationary eigenstates [31]. A wave packet is the wave-function manifestation of a non-stationary state. The mathematical form of such statement is given in the following equation:

$$|\psi(t)\rangle = \sum c_n |\psi_n\rangle e^{-iE_n t/\hbar} \tag{1.12}$$

where $|\psi\rangle$ is the wavefunction of a non-stationary state, $|\psi_n\rangle$ and E_n denote the wavefunction and energy of the stationary eigenstate designated by the quantum number n and c_n is the normalized probability amplitude. Contrary to a stationary state whose energy is certain and fixed at any given time t, the energy of a non-stationary state is indeterminate. At any given time, the system can exist in any of its stationary states with its corresponding energy. A measurement of the system would result in finding the system in one of the stationary states and the probability of finding the system in stationary state n is given by $|c_n|^2$. The commonly used spectroscopic method in frequency domain measures the system when it "collapses" into a single stationary state whose energy is certain, whereas the quantum beating experiment is able to characterize the time-resolved non-stationary states.

We illustrate the basic principles of quantum beating by looking at a simple four-level system as shown in Figure 1.7.

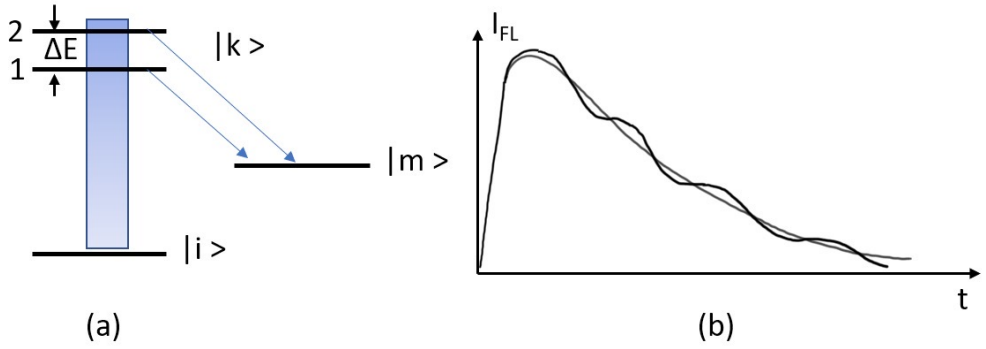

Figure 1.7: (a) A four-level system to illustrate quantum beating. (b) The intensity of fluorescence decay from the two coherently excited levels plotted in time domain.

In Figure 1.7, if two states $|1\rangle$ and $|2\rangle$ are simultaneously excited from the same initial state $|i\rangle$ at time t= 0 by a sufficiently short laser pulse whose

bandwidth is wide enough to cover the energies of both states $|1\rangle$ and $|2\rangle$, the coherent superposition of the two states at t=0 becomes

$$\psi(t=0) = \sum c_n \psi_n = c_1|1\rangle + c_2|2\rangle \tag{1.13}$$

After the excitation, if the population from the two levels decays to a lower level $|m\rangle$ with a decay constant $\gamma_n = 1/\tau_n$, the wavefunction of the superposition state evolves over time according to [16]

$$\psi(t) = \sum \psi_n e^{-(i\omega_{nm}+\gamma_n/2)t} \tag{1.14}$$

where $\omega_{nm} = (E_n - E_m)/\hbar$. So each eigenstate in the originally excited wave packet not only decays to level $|m\rangle$, manifested as the exponentially decreasing probability of finding the system in state n, but also has an oscillating phaser whose angular frequency changes from ω_n to ω_{nm}. The oscillating angular frequency ω_{nm} corresponds to the energy difference between the originally excited eigenstate $|n\rangle$ ($n = 1$ or 2) and the final state $|m\rangle$, although the changed frequency is not directly observable in the measurement so far. What can be directly monitored is the intensity of the fluorescence during the decay. If the detector measures the fluorescence of the decay from the total wave packet without distinguishing between the initial state 1 and 2, the intensity measured on the detector can be given as a function of time,

$$I(t) = C \mid \langle m|\boldsymbol{\epsilon} \cdot \boldsymbol{\mu}|\psi(t)\rangle \mid^2 \tag{1.15}$$

where C is a constant representing the response of the detector, ϵ is the polarization vector of the emitted field and $\boldsymbol{\mu} = e \cdot \mathbf{r}$ is the electric dipole moment. Assuming equal decay rate $\gamma_1 = \gamma_2 = \gamma$ and inserting Equation 1.14 into Equation 1.15, the intensity of the emission measurable on the detector becomes

$$I(t) = Ce^{-\gamma t}(A + Bcos(\omega_{21}t)) \tag{1.16}$$

where

$$\omega_{21} = \frac{E_2 - E_1}{\hbar} \tag{1.17}$$

and

$$
\begin{aligned}
A &= c_1^2 \mid \langle m|\boldsymbol{\epsilon}\cdot\boldsymbol{\mu}|1\rangle \mid^2 + c_2^2 \mid \langle m|\boldsymbol{\epsilon}\cdot\boldsymbol{\mu}|2\rangle \mid^2 \\
B &= 2c_1c_2 \mid \langle m|\boldsymbol{\epsilon}\cdot\boldsymbol{\mu}|1\rangle \mid \cdot \mid \langle m|\boldsymbol{\epsilon}\cdot\boldsymbol{\mu}|2\rangle \mid
\end{aligned}
\tag{1.18}
$$

We can see from Equation 1.16 that in addition to the exponentially decaying term that can be measured on the detector, the decaying intensity is also modulated (see Figure 1.7 (b)) by a cosine term whose angular frequency $\omega_{21} = (E_2 - E_1)/\hbar$ represents the exact energy spacing between the two initial coherently excited states $|1\rangle$ and $|2\rangle$. The root cause of this modulation is from the interference between the time-dependent wave functions of the two eigenstates that are coherently excited initially. The observable oscillation looks like a "beat" between the oscillating frequencies of each individual eigenstate. Thus the phenomenon is called quantum beating. Fourier analysis of the data measured in time domain should yield the spectrum in frequency domain on which quantum beating frequencies can be identified. This is the quantum beating spectroscopy.

As quantum beating is an inherently Doppler-free spectroscopic technique [33], it is immediately beneficial to the study of atomic and molecular spectroscopy, particularly the study of fine or hyperfine splitting, Lamb shifts, fine rotational or vibrational structures, ranging from typically a few MHz [34] to more than a hundred of MHz [35]. A typical quantum beat measurement in time domain and its Fourier spectrum are shown in Figure 1.8 [32]. Two superimposed quantum beats can be seen on the Fourier domain spectrum, separated by 200 kHz, and resulted from two sets of two coherently excited levels in the six-atomic molecule propynal.

The linewidth of the quantum beat spectrum is limited not by the linewidth of the laser and Doppler-broadening, but by homogeneous broadening. Assuming the excited states have much longer lifetime than the timescale for quantum beat observation, the homogeneous broadening is composed of the collisional broadening and the diffusion of oriented atoms out of the interaction zone [16]. The two can be competing factors to determine the quantum beat linewidth, although adding noble gases should slow down the diffusion, revealing more of the collisional broadening part.

Since the frequency of the quantum beat corresponds to the energy difference between the coherently excited eigenstates in a wave packet, the largest

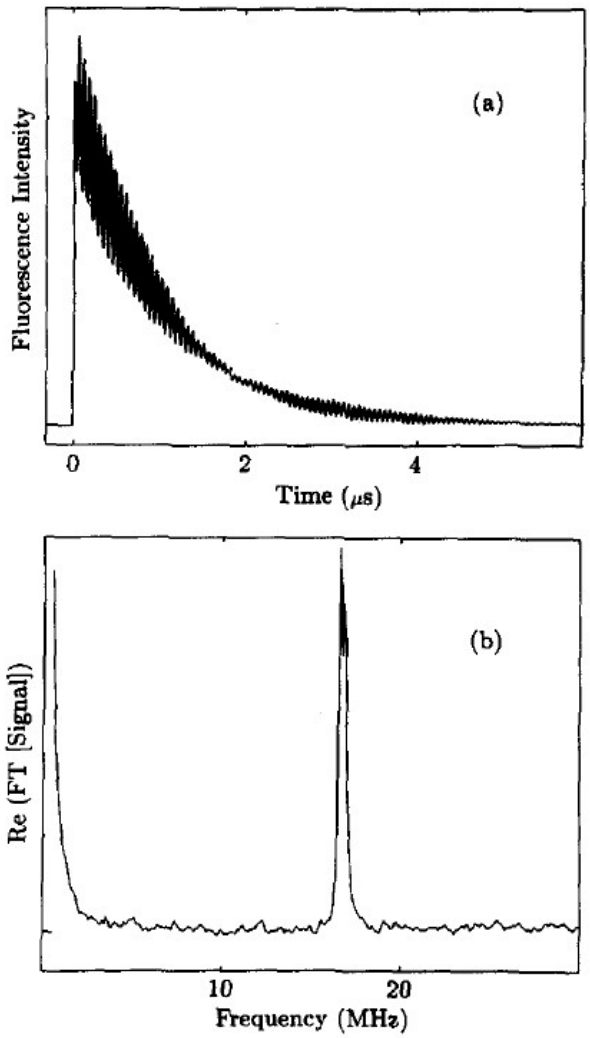

Figure 1.8: Example of a quantum beat measurement. (a) Quantum beats in the fluorescence decay (time domain) of the 5_0^1 band of S^1 propynal (six-atomic molecule). (b) The real part of the Fourier transform in frequency domain. Reprinted from [32], with permission from Elsevier.

quantum beat frequency observable is limited by the bandwidth of the coherent excitation source. According to Fourier transform, to coherently excite the two stationary states in Equation 1.13, the duration of the laser pulse has to be shorter than $\delta t \leqslant \hbar/(E_2 - E_1)$. As we shall see soon, in order to observe THz-range quantum beats between widely separated atomic levels at low principal quantum numbers, femtosecond laser sources become necessary, which did not become available until the 1980s.

1.2.2 Parametric Four-Wave Mixing (PFWM) and Pump-Probe Experiment

Even with the ultrafast laser source available, observing quantum beats at THz still imposes a challenge - optical detector cannot respond fast enough to record the THz oscillations. This problem can be solved by conducting a pump-probe experiment, which we discuss now.

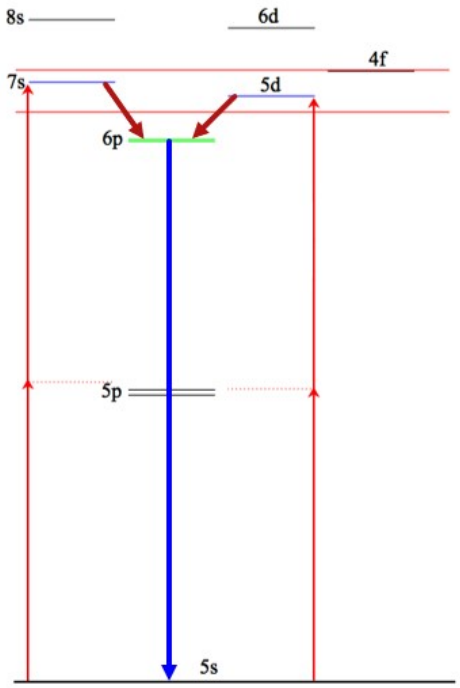

Figure 1.9: Energy levels in Rb and the illustration of parametric four-wave mixing (PFWM) process.

Some energy levels of Rb are shown in Figure 1.9. We want to observe the quantum beating between the $7s$ and $5d$ states in Rb, which has an energy spacing of 18.2 THz ($\times h$ to convert to Joules). This oscillation is too fast to be recorded on common detectors. Instead of exciting both energy levels once and then observing the decaying emission from them, we split one laser pulse into two beams, one designated as the pump beam and the other as the probe beam. We set an optical delay between the pump and probe beam, and the delay can be varied. For each laser pulse, the pump beam first excites the $7s$ and $5d$ energy levels at time t=0, preparing the wave packets. After a delay, the probe beam reaches the sample again, initiating a nonlinear process parametric four-wave mixing (PFWM) [36](see Figure

1.9), which simultaneously generates a signal wave as the emission from $6p$ state to $5s$ state, and the idler waves as the emission from $7s$ or $5d$ state to $6p$ state. The intensity of the signal wave emission ($6p \rightarrow 5s$) depends on the instantaneous property of the temporally evolving non-degenerate wavepacket when the probe beam reaches the sample, and thus depends on the temporal delay between the pump and probe beam. Since the emission from $6p$ to $5s$ state cannot distinguish between its origin from $7s$ and $5d$ state, the scenario is very similar to the process described in Figure 1.7(a). In this way, each pump-probe pair of laser beams should have a different temporal delay, which can be defined by varying the length difference between the two beams' correspondent optical paths. Each delay can be manually set before firing each pair of the pump-probe beam, so one should have plenty of time to set the delay. If we record the intensity of $6p$-$5s$ emission as a function of the pump-probe delay, we can again observe the quantum beating similar to Figure 1.7(b). The pump-probe setup in combination with PFWM thus eliminates the need of THz response for the optical detector and electronics, because a manually controllable pump-probe delay takes over the duty of tracing the system's natural temporal response. This only illustrates the principle of pump-probe experiment via PFWM. The actual experimental setup will be discussed in Chapter 2.

Eden's group at University of Illinois made great effort in refining the PFWM-based quantum beating experiments in the last decades. Tran *et al.* first applied femtosecond laser to coherently excite wavepackets between widely spaced alkali atomic energy levels at low principal quantum numbers and observed the THz quantum beats [37, 38]. Oldenburg [39], Spinka [40] and Ricconi [41] further verified that the observed optical signal was due to the PFWM process, and introduced improved quantum mechanical analytic models. The processes were better understood in theory and the influence of laser pulse parameters such as bandwidth, chirp or energy density was investigated. Senin [42, 43] and Xiao [44, 45] applied the PFWM-based quantum beating technique to the observation of dissociation dynamics of near-range Rb_2 molecules (versus long-range as is the subject of this dissertation), by analyzing the pressure-dependent temporal behavior of the atomic quantum beat ($7s$-$5d$).

Accompanying these discoveries at Eden's group is the continuous improvement of the signal-to-noise ratio (SNR) of the observed quantum beat signal

as a result of laser improvement and optimization of the optical system and the data acquisition system. This drastic improvement in SNR enables us to observe features on the quantum beat spectrum that were not observed before, including the vibrational structure of the long-range Rydberg molecules (LRRMs). Chapter 2 explains in details the experimental setup and Chapter 3 presents the quantum beating LRRM observations and analysis.

CHAPTER 2

THE EXPERIMENTAL SETUP

In order to observe quantum beating between rubidium atomic energy levels and the associated long-range Rydberg molecular structure, the experimental setup requires four basic functional blocks on a system level: a coherent broadband light source, an interferometer to introduce pump-probe delay, a rubidium vapor sample assembly and a signal detection system.

A simplified schematic of the experimental setup is illustrated in Figure 2.1. The femtosecond laser serves as the coherent light source that has a bandwidth wide enough to excited both Rb $7s$ and $5d$ atomic states simultaneously. Each laser pulse is split into the pump and probe beam in a interferometer configuration, with an adjustable delay between the pump and probe beam by putting the probe beam mirrors on a linear stage. The pump and probe beam thus sequentially interact with the rubidium vapor, contained within a glass cell heated by a temperature-controlled oven. The coherent optical emission corresponding to the energy difference between Rb $6p$ and $5s$ states is produced by the non-linear parametric four-wave mixing (PFWM) process (see Figure 1.9) and is filtered and collected by the photomultiplier tube (PMT). The signal is digitalized and sent to the computer for analysis.

The first part of this chapter discusses each of the four functional blocks in the experimental setup. The descriptions of the light source, interferometer and rubidium vapor assembly are limited to minimum technical details. The information presented here is to help the reader understand the experimental setup and critical experimental parameters that will influence the study of long-range Rydberg molecules. The reader can find additional technical details in William Goldshlag's dissertation [46] should the need arise.

For the fourth functional block, the signal detection system, we have developed two different methods to acquire the data. The first data acquisition (DAQ) method is based on an off-the-shelf DAQ module from National In-

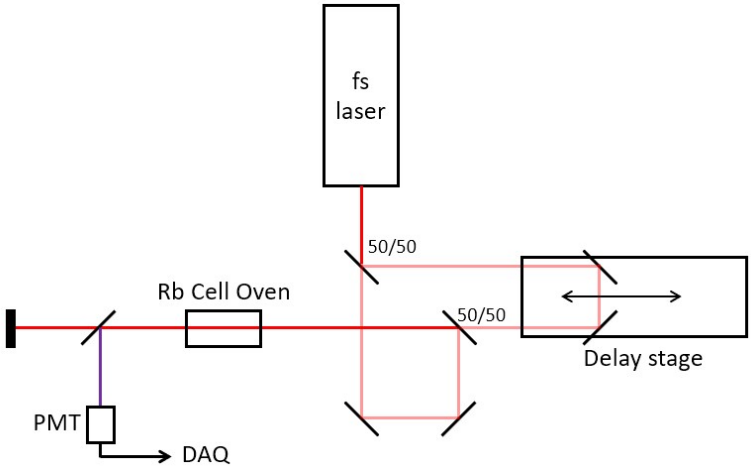

Figure 2.1: Simplified schematic of the experimental setup. PD: photodiode. PMT: photomultiplier tube. Each laser pulse is split into the pump and probe beams. The pump-probe delay can be varied by moving the linear stage on which mirrors of the probe beam path are located.

struments (NI) in combination with William Goldshlag's LabView programs. We will discuss this method at a high level but the reader can refer to William Goldshlag's dissertation [46] for more technical details. The second method is a newly developed DAQ system based on field-programmable gate array (FPGA). This second method yields lower signal-to-noise ratio (SNR) than the first method, but is 300 times faster. Both methods are employed in the work for different purposes. The second part of this chapter will introduce in detail the FPGA-based DAQ method and discuss the trade-offs in choosing between the two methods for experiments.

2.1 The Quantum Beating Experiments Platform

Femtosecond pulses are generated by a commercial custom-built femtosecond laser system from Coherent Inc. that is composed of an oscillator and a regenerative amplifier. The oscillator, Vitara-T, is pumped by an integrated optically pumped semiconductor laser Verdi-G (532 nm). Oscillator Vitara-T is able to produce 80 MHz, more than 400 mW average power of near-infrared pulses with pulse duration of less than 12 fs and bandwidth (FWHM) of 30-125 nm. An output spectrum of Vitara-T used in our experiments is shown in Figure 2.2. The 80 MHz, 5 nJ/pulse oscillator output is amplified and

converted into 1 kHz, 2-3 mJ pulses by the Ti:sapphire regenerative amplifier Coherent Legend Elite HE+. The normalized output spectra of the stretcher, regenerative cavity and compressor are shown in Figure 2.2. The output pulses leaving the femtosecond laser system have a center wavelength of 768 nm and FWHM of 20 nm. The blueshift of the center wavelength from the peak gain of 800 nm of the Ti:sapphire crystal is due to the custom coatings of the regenerative cavity mirrors and an added intracavity narrow-band filter. This shifting of the spectrum is done on purpose to better accommodate the excitation of Rb $7s$ and $5d$ atomic states. It is worth noting that by adjusting a motorized translation stage under the compressor grating, some degree of non-linear chirp can be introduced and the laser output can be adjusted away from the optimal transform-limited condition (55 fs in time domain). In Chapter 3 we will see that the optimal condition to get the largest quantum beating signal between $7s$ and $5d$ states is not when the laser output is transform-limited, but when the laser output is negatively chirped. The chirp of the laser is monitored and adjusted with the assistance of frequency-resolved-optical-grating (FROG).

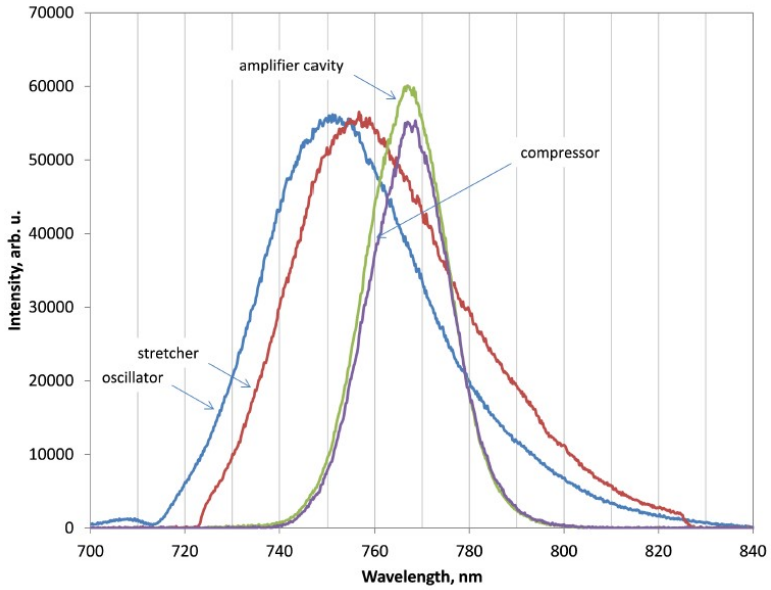

Figure 2.2: Normalized spectra of the femtosecond laser system. **oscillator:** Vitara-T output, **stretcher:** Legend Elite HE+ stretcher output, **amplifier cavity:** regenerative cavity output, **compressor:** laser output. Reproduced with permission from William Goldshlag's PhD dissertation [46].

After a femtosecond pulse is generated, it enters the Michelson interferometer where it is split into two identical pulses with a delay between them controlled by the linear translation stage (Physik Instrumente PI-M521.DDB) of one arm of the interferometer. The fixed delay arm produces the pump pulse and the varied-delay arm produces the probe pulse. The optical paths of the pump and probe pulses are later recombined so that they propagate colinearly towards the Rb sample cell.

The maximum delay between the pump and probe beam is about 1100 ps, limited by the maximum travel range of the linear stage. The linear stage has an encoder resolution of about 0.1 μm, corresponding to 0.66 fs temporal resolution of the delay. A typical step size of the scan we used is about 0.5 μm, corresponding to a sampling period of 3.33 fs and a sampling frequency of about 300 THz. The Nyquist frequency is much larger than the frequencies of the quantum beating signals that we are looking at.

The pump and probe beam thus sequentially interact with the rubidium vapor, contained within a glass cell heated by a temperature-controlled oven. A picture of the glass cell containing the gas vapor is shown in Figure 2.3. The glass cell is composed of two hollow glass cylinders connected with each other in a T-shape. The upper horizontal cylinder encloses the optical path and is 25 mm long with 12.5 mm outer diameter and the vertical "stem" cylinder is only 6.4 mm in outer diameter. The windows at the two ends of the upper cylinder are tilted at a slight angle (11°) to remove reflections propagating along the optical axis. The two cylinders are heated independently and the "stem" cylinder is kept 25 °C lower than the upper cylinder. The "stem" cylinder thus serves as a "cold finger" whose temperature controls the gas number density of the unsaturated rubidium vapor and prevents the deposition of rubidium vapor onto the side walls of the upper cylinder. The temperatures of the "cold finger" we used in our experiment span from 413 K to 543 K, corresponding to Rb number densities of (0.6-100)$\times 10^{14}$ cm^{-3}.

For each pair of pump and probe pulses, the pump pulse reaches the rubidium cell first, exciting Rb atoms from ground state to both $7s$ and $5d$ states through two-photon excitation. Upon excitation, the wavefunctions of $7s$ and $5d$ states are generated and evolve over time even after the pump pulse ceases. After a certain delay, the probe pulse reach the rubidium cell, coherently generating $6p$-$5s$ emission through the nonlinear parametric four-wave mixing (PFWM) process (see Figure 1.9). The intensity of the emitted

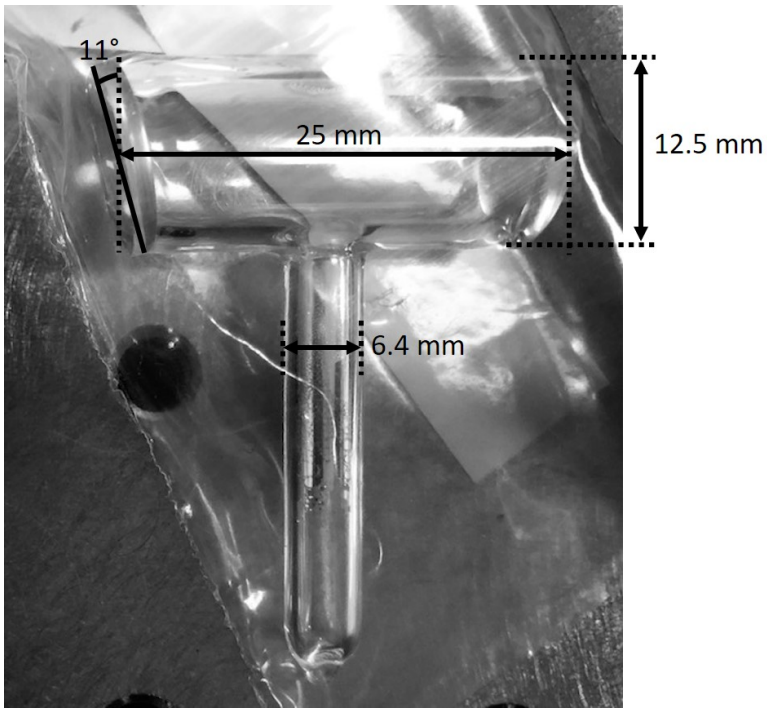

Figure 2.3: An annotated photo of the gas cell containing rubidium vapors. The upper horizontal cylinder encloses the optical path and is 25 mm long with 12.5 mm outer diameter, and the vertical "stem" cylinder is 6.4 mm in outer diameter. The windows at the two ends of the upper cylinder are tilted at a slight angle (11°) to remove reflections propagating along the optical axis. The lower cylinder is kept 25 °C lower than the upper cylinder to prevent deposition on the inside of the upper cylinder.

$6p$-$5s$ light depends on the time delay between the pump and probe pulse, as the emission reflects the temporal evolution of the $7s$ and $5d$ wavefunctions. The working principles of the quantum beating experiment conducted in a pump-probe configuration utilizing PFWM were introduced in Chapter 1.

As the quantum beating signal of the $6p$-$5s$ emission at 420 nm co-propagates with the probe pulse and other idler signals in PFWM, it is separated by a dichroic mirror and passes through a narrow-band filter to further remove residuals of light from the laser before entering the photomultiplier tube (PMT). For each pair of the pump and probe beams, the current signal generated by PMT is converted to voltage and sent to a boxcar integrator (Stanford Research Instruments SR-250) with proper impedance match. The boxcar converts a transient signal into a steady voltage ready to be sampled by the data acquisition system. The output of the boxcar either goes into a commercial data acquisition module (DAQ, National Instruments NI-6009) to be used with LabVIEW, or into the analog-to-digital converter (ADC) embedded within an FPGA chip (Xilinx Artix-7), depending on the two different modes of scan we are going to talk about.

In the case of using NI DAQ module in combination with LabVIEW programs developed by William Goldshlag [46], for each new sampling point to take, the program commands the stage to move to a new delay position, wait 250 ms for the stage to stabilize, then sample the data with a delay to the next trigger of the laser. Because at each time when the data is taken the stage is stopped completely, this scanning regime provides superior signal-to-noise ratio (SNR). However, because of the 250 ms stabilizing time for each data point, for the 1000 laser pulses within a second, at most 4 pulses can be utilized. In addition, the actual acquisition rate is also impeded by the inherent speed limitations of LabVIEW. In conclusion, this method yields excellent SNR but each full scan will take approximately 17 hours to get the desired frequency resolution. In order to speed up the data acquisition in certain cases, I developed a second method based on FPGA.

2.2 FPGA-based High-speed Scan Method

The second scanning system utilizes a custom-designed digital circuits in FPGA for data acquisition. The linear stage is commanded to move at a

constant speed unstoppingly during the scan and the sampling points are determined by the triggering of the laser pulses which are equally spaced in time (the jittering of the trigger was tested and is negligible when compared with the sampling period). Because this system eliminates the 250 ms waiting time for each new delay position, and the custom-made digital circuits in FPGA run more efficiently than Labview on PC, one scan now takes less than 4 min, which is about 300 times faster than the first system.

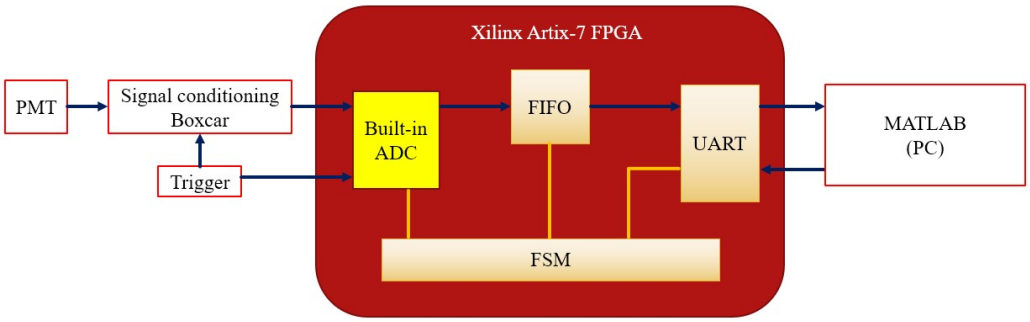

Figure 2.4: Schematic of the custom-made FPGA-based scanning system. ADC: analog-to-digital converter. FIFO: first-in-first-out buffer. UART: universal asynchronous receiver-transmitter. FSM: finite state machine. The ADC shares the same trigger with the femtosecond laser so the stage can move unstoppingly during the scan.

A schematic of this FPGA-based scanning system is shown in Figure 2.4. The on-chip analog-to-digital converter (XADC) is part of the Xilinx Artix-7 FPGA (XC7A100T-1CSG324C) and can be configured and integrated with the rest of the digital circuits through configuring its intellectual property core (IP core). The XADC samples the voltage at the output of Boxcar for each data point at the trigger from the delay generator that also triggers the generation of laser pulses (1 kHz). The digitalized data are then sent to the PC through the universal asynchronous received/transmitter (UART) core developed on FPGA. The FPGA chip is part of the Nexys4 DDR development board which also includes a USB-UART bridge and a shared UART/JTAG port so that PC can directly communicate with the board using standard Windows COM port commands. The UART core not only sends acquired data to PC but also receives commands from PC to start the acquisition progress or configure certain acquisition parameters.

An additional first-in-first-out (FIFO) core is developed to serve as a buffer between the output of XADC and UART because the output data of XADC

Table 2.1: Comparison between the high-accuracy and high-speed scanning methods.

	High-accuracy Method	High-speed Method
DAQ device	NI DAQ module	Xilinx Artix FPGA
ADC resolution	16 bit	12 bit
Linear stage moving mode	Move and stop	Move continuously
DAQ rate	3 Hz	1000 Hz
Full-scan time	17 hours	4 min
Can use coherent averaging to increase SNR?	Yes, usually 20 sets	No

needs to be serialized by the UART core before being sent to PC.

Finally, a finite state machine (FSM) is developed to control the data flows between XADC core, FIFO core and UART core. A block diagram of the whole system is shown in Figure 2.5. An algorithmic state machine (ASM) chart on a high level is shown in Figure 2.6.

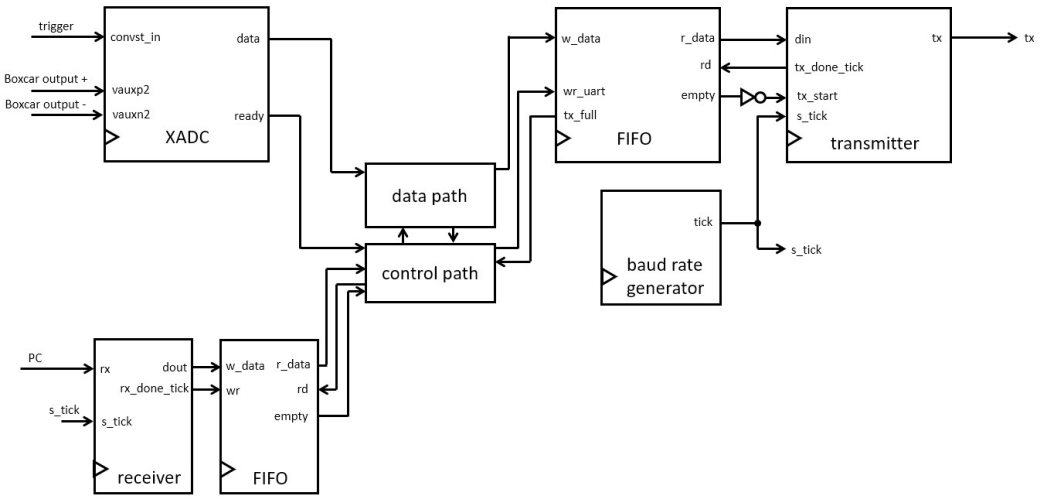

Figure 2.5: Schematic of the block diagram of the system.

2.3 Comparison between the High-accuracy and High-speed Scanning Methods

Table 2.1 shows the comparison between the NI-LabVIEW high-accuracy scanning method and the FPGA-based high-speed scanning method. Be-

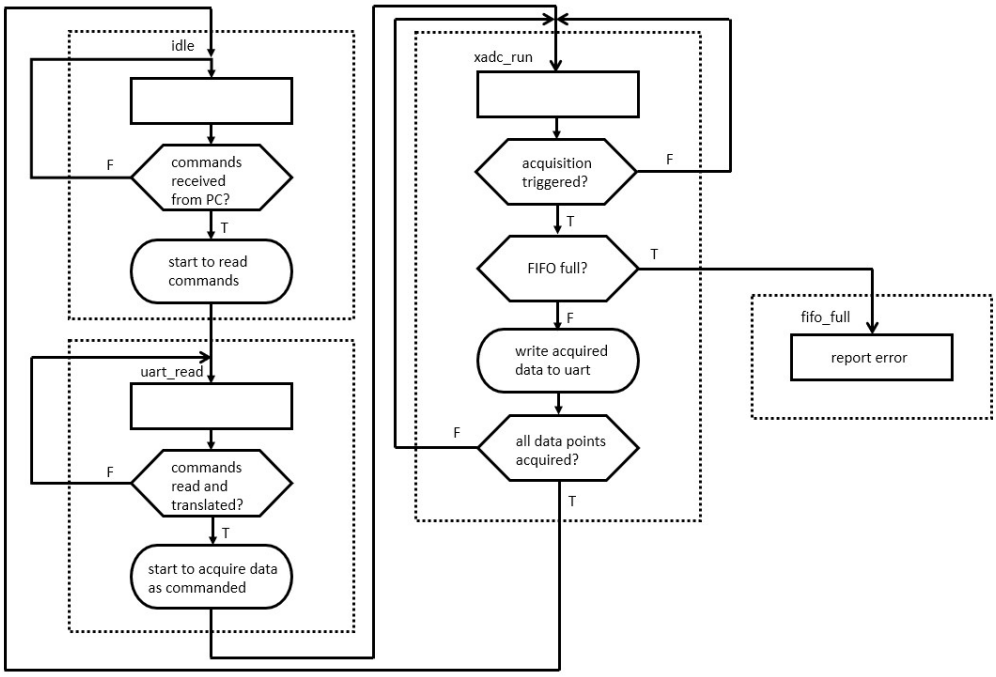

Figure 2.6: ASM chart of the finite state machine (simplified at high level, real chart is far more complicated).

cause the high-accuracy method stops the stage completely each time when it moves to a new position, it cannot acquire the data at more than 3 Hz. Each full scan will take more than 17 hours to finish. Because the stage stops at each new position, the system can take multiple data points to do coherent averaging. As we know that the SNR of DFT is proportional to $\sqrt{N}$ where N is the number of data points taken for coherent averaging, the high-accuracy method not only increases SNR due to its excellent stage stability but also can benefit from coherent averaging. In the high-speed method, however, because the stage has to move continuously and for each scan the temporal reference is random, this method is fast but cannot take advantage of coherent averaging to increase SNR. In addition, due to physical limitations the linear stage cannot move at perfectly constant speed. A plot of the stage position versus time reported by the linear stage firmware is shown in Figure 2.7. We see that the plot is not perfectly a straight line. Defects of the stage add additional positioning uncertainties, or jitter. As the data acquisition is triggered by the laser delay generator, which demonstrates negligible jitter between pulses, this jitter in the stage positioning implies that the increments in the pump-probe delay are not perfectly equal. In other words, the

temporal evolution of the rubidium wavefunctions is not sampled at equal spacing in time, which further reduces the SNR of the DFT spectrum. On the other hand, as the high-speed method reduces a 17 hour scan to less than 4 min, it drastically increases the repeatability and fidelity of the data by reducing various environmental and apparatus drifting factors that influence the signals in a 17 hour scan. The high-speed method can sense very small change in quantum beating signal caused by the change in experimental parameters or conditions, such as the laser intensity, chirp, crossing angles between the pump and probe beam, etc. As a result, the high-speed method is particularly helpful for the determination of the optimal condition for generating strong quantum beat signal, as will be demonstrated in Chapter 3. In summary, the two scanning methods have their own trade-offs. It is easy to switch between the two methods and we use them both depending on the need.

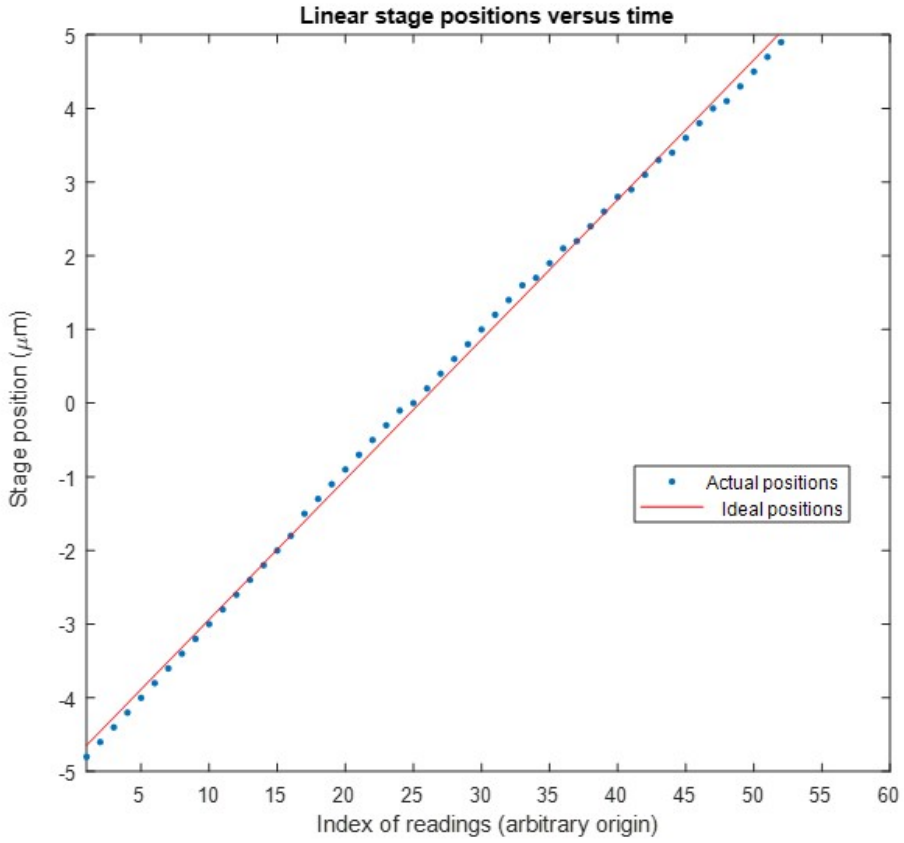

Figure 2.7: Linear stage position versus time reported by the stage firmware. Ideally the stage is supposed to move at constant speed so the plot should be perfectly linear. But defects of the stage add uncertainties to the stage movement.

CHAPTER 3

EXPERIMENTAL DATA AND ANALYSIS

Quantum beats between rubidium atomic levels and vibrational levels of long-range Rb_2 were both observed in the rubidium gas vapor with natural abundance by pump-probe experiments. This chapter presents the details of experimental data and their analysis.

Specifically, quantum beating between rubidium $7s$ and $5d_{5/2}$ atomic states is observed by monitoring the emission intensity of $6p_{3/2} \rightarrow 5s_{1/2}$ transition as a function of the pump-probe delay. Additionally, quantum beating between $8s$ and $6d_{5/2}$ atomic states is also observed despite the fact that $8s$ and $6d_{5/2}$ states are not directly excited. Using the high-speed scanning method discussed in Chapter 2, the optimal experimental conditions for producing the strongest quantum beating signals are found and discussed. Other features are also observed on the frequency-domain spectrum in addition to the main $7s$-$5d_{5/2}$ and $8s$-$6d_{5/2}$ quantum beating peaks. First, multiple harmonics and the sum and difference of the these fundamental quantum beating frequencies are observed, indicating strong nonlinearity of the system. Second, series of overtones are observed on each side of the main $7s$-$5d_{5/2}$ and $8s$-$6d_{5/2}$ quantum beating peaks. Analysis indicates these overtones originate from the long-distance Rydberg molecular structure of rubidium. Specifically, each fundamental frequency of the overtones corresponds to the energy spacing between the vibrational energy levels within the quantum wells on the potential curves of long-range Rb_2. Vibrational constants are derived from these series and are found to be similar to previous experimental studies in the literature. Dissociation energies of these quantum wells were calculated and found to be within one order of magnitude of the values extrapolated from other data that were published. Last but not least, comparing the quantum beat spectrum obtained from rubidium vapor, rubidium-argon mixture and rubidium-cesium mixture shows that different ground state perturbers exert different effects on the formation of LRRM.

Quantum beat spectroscopy (QBS) is employed to study long-range Rydberg molecules (LRRM) for the very first time. Our data show that QBS serves as a special tool in the investigation of LRRM not only for its simplicity in implementation, compared with more commonly used Bose-Einstein condensates combined with precision laser scan and field ionization methods, but also for its several distinctive advantages, such as its broad excitation bandwidth and its versatility to study alkali-RG(rare gas) heteronuclear long-range molecules. We will discuss in more detail the special advantages and novelties of using QBS to study LRRM after the analysis of data.

3.1 Rubidium Quantum Beating between Atomic Levels

The wave packets composed of Rydberg states $7s$ and $5d_{5/2}$ are coherently excited by the pump pulse and their temporal evolution is interrogated by the probe pulse. The intensity of emission from $6p$ state to $5s$ is plotted as a function of the pump-probe delay t as shown in Figure 3.1. The resolution in time (or sampling period) is 3.33 fs (see inset of Figure 3.1), corresponding to 0.5 μm in the step size of stage movement and sampling frequency f_s of 300 THz (or a Nyquist frequency of 150 THz). According to Nyquist theorem [47], this guarantees sufficient sampling of signals smaller than 150 THz. The majority of the quantum beating frequencies we are trying to study are way below 150 THz.

With a sampling period of 3.33 fs, 200,000 data points (or pump-probe delays) are taken. This means that the maximum pump-probe delay sampled is about 650 ps. The frequency resolution of the discrete Fourier transform (DFT) is given by [48]

$$\delta F = \frac{f_s}{N} \tag{3.1}$$

where N is the number of samples taken. According to Equation 3.1, the resolution of the DFT is proportional to the number of the sampling points N and inversely proportional to the sampling frequency f_s. The sampling frequency f_s is governed by the Nyquist theorem and N is limited by the total travel length of the linear stage. With f_s of 300 THz and N of 200,000, the frequency resolution of the DFT is about 1.5 GHz or 0.05 cm^{-1} without

zero padding. In addition, for each pump-probe delay, 20 samples are taken for coherent averaging [49] to increase SNR.

Unless mentioned otherwise, most of the data being presented in this chapter were obtained under the following experimental conditions: The pump and probe pulses of the laser beam are of equal intensity at 150 μJ. This intensity is measured right after the beams come out of the oven, so the actual laser beam intensity inside the gas cell could be stronger, taking into account the deflection and scattering of the beams inside the oven. The temperature at the "cold finger" of the cells is 443 K (170 °C), corresponding to a Rb number density of 2.5×10^{14} cm^{-3}.

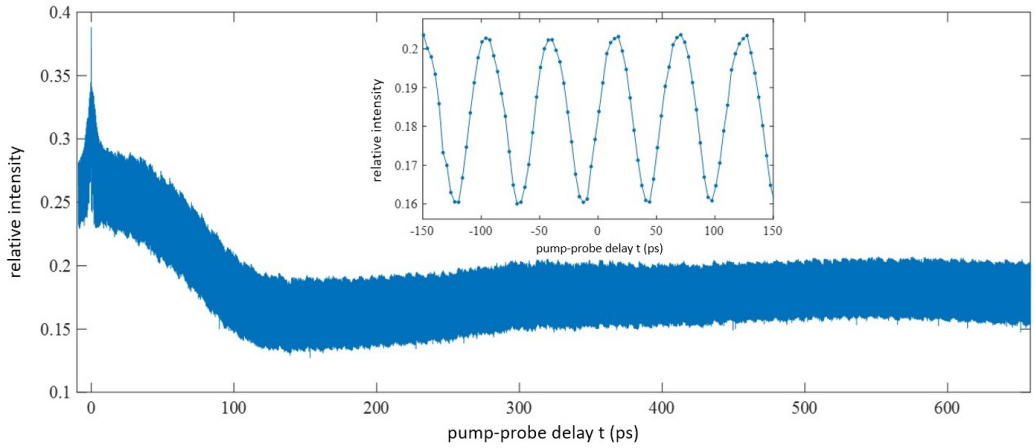

Figure 3.1: $6p$-$5s$ emission intensity as a function of pump-probe delay in the quantum beating experiment. Inset is a zoomed-in view around 500 ps. Note that the origin of the abscissa of the inset is chosen arbitrarily.

The inset of Figure 3.1 shows a zoomed-in view of the plot around 200 ps. The origin of the abscissa of the inset is chosen arbitrarily. From the inset we see that the temporal evolution of the signal roughly resembles a sinusoidal wave with an oscillating period of roughly 55 fs, or about 18.2 THz, which corresponds to the energy spacing between the 7s and 5d states. As we will soon present, after taking the DFT a strong peak can be observed in the frequency domain whose oscillation frequency corresponds to the energy difference between $7s$ and $5d$ states with an error of only 0.02% when compared with the NIST data. Secondly, a periodogram with calculated total harmonic distortion (THD) is shown in Figure 3.2. Total harmonic distortion [50] is a

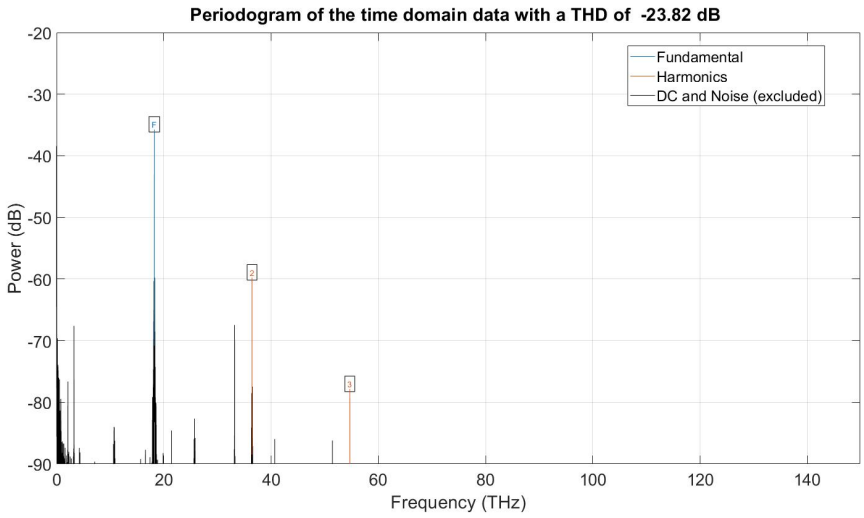

Figure 3.2: Periodogram and total harmonic distortion (THD) of the time-domain signal. The sampling frequency is at $\approx$ 300 THz and a strong fundamental mode is found at $\approx$ 18.225 THz. The THD is determined from the fundamental frequency and the first five harmonics. Its definition is given in the text. Note that the ordinate of the graph is logarithmic.

measurement of the harmonic distortion present in a signal and is given by

$$\text{THD} = 10 \times \log(\frac{V_2^2 + V_3^2 + V_4^2 + ...}{V_1^2}) \tag{3.2}$$

where V_n is the RMS voltage of the nth harmonic and $n = 1$ is the fundamental frequency. A THD of -23.82 dB indicates a strong signal at the fundamental frequency when compared with higher order harmonics. From the periodogram we see that the frequency components of the time-domain data are dominated by the strong peak at 18.225 THz and its higher harmonics (the ordinate of the graph is logarithmic), despite the fact that there are other noticeable frequency components. We will further analyze the frequency components in the frequency domain by taking the DFT. Last but not least, in the time domain (Figure 3.1) we see stronger signals around time t=0, especially at t=0, where the pump and probe beams overlap with each other. The strong interference when the pump and probe beam overlap increases the baseline of the signal intensity, possibly because of strong near-continuous wavepackets excitations. In fact, we determine the zero pump-probe delay by looking around the vicinity of the strongest signal baseline. A plot showing the signal behavior around zero pump-probe delay is shown

in Figure 3.3.

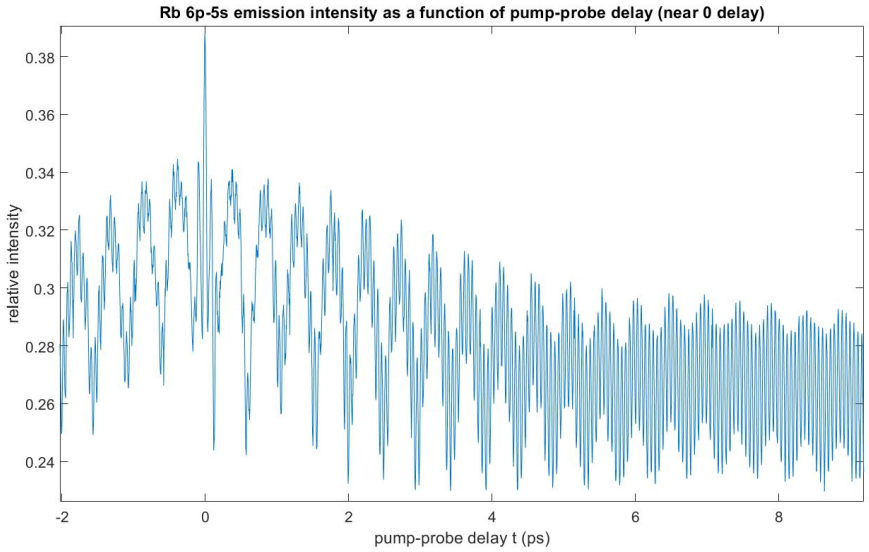

Figure 3.3: $6p$-$5s$ emission intensity as a function of pump-probe delay near the 0 delay. Notice the elevated overall signal baseline and the symmetric Ramsey fringes near 0 time delay.

Applying discrete Fourier transform (DFT) to the time-domain data yields the quantum beating spectrum in the frequency domain which is shown in Figure 3.4. A zoomed-in view of the spectrum is shown in Figure 3.5 which demonstrates the lower-magnitude structure of the spectrum. We see that a plethora of quantum beating peaks were generated in the experiments. Most peaks on the spectrum belong to one of the following categories:

1. Peaks whose frequencies correspond to the energy difference between atomic levels and multiple higher order harmonics of these fundamental frequencies. The fundamental frequencies are:

   - Energy difference between Rb $7s$ and $5d_{5/2}$ at 18.225 THz ($7s$ - $5d_{5/2}$). These two levels are expected to be excited by the laser through two-photon process.
   - Energy difference between Rb $8s$ and $6d_{5/2}$ at 10.726 THz ($8s$ - $6d_{5/2}$. These two levels are not accessible through one photon or two-photon excitation processes by the laser.

2. The difference between two energy differences ($5d_{5/2}$-$5p_{3/2}$)-($5p_{3/2}$-$5s_{1/2}$) at 2.11 THz. Spectrograms yielded by short-time Fourier transform

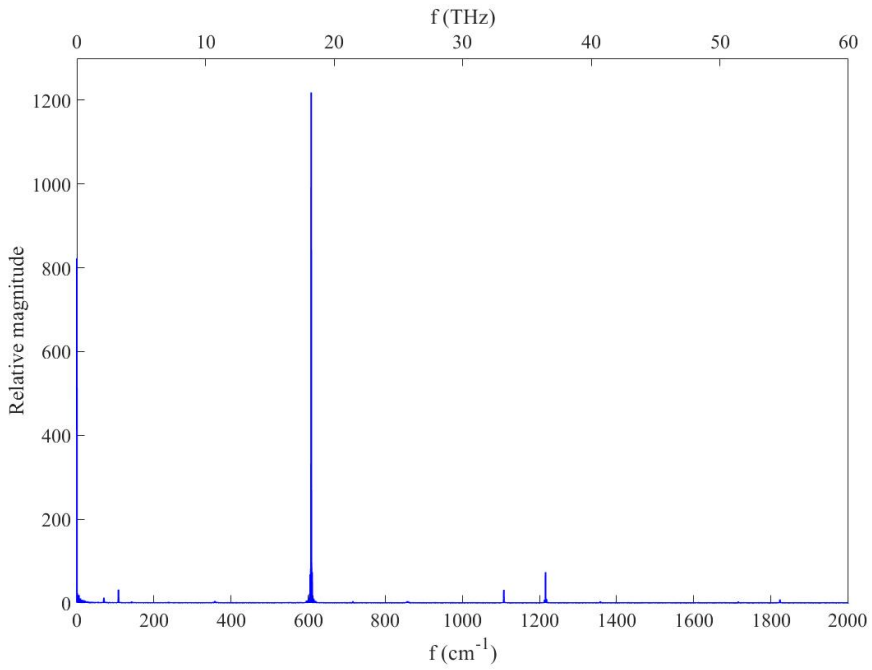

Figure 3.4: Panoramic view of the quantum beating spectrum. The dominant peak at 18.225 THz corresponds to the 55 fs oscillation period in time domain and the energy difference between $7s$ and $5d_{5/2}$ state.

show that this beating peak decays quickly, within the first 100 ps after the zero pump-probe delay.

3. Multiples of a fundamental frequency (overtones) which corresponds to the frequency difference between 18.225 THz and 10.726 THz (see the first category), appearing on both sides of the 18.225 THz peak. In order words, frequencies can be found given by

$$\nu_N = (7s - 5d) \pm N\Delta \tag{3.3}$$

where N is an integer 0, 1, 2, ... and Δ denotes the difference between the two frequencies from category 1, namely,

$$\Delta = (7s - 5d) - (8s - 6d) \approx 250.2\,\mathrm{cm}^{-1} \tag{3.4}$$

A summary of all the identified peaks, in comparison to the NIST data, is shown in Table 3.1. Quantum beating between $7s$ and $5d_{5/2}$ states and

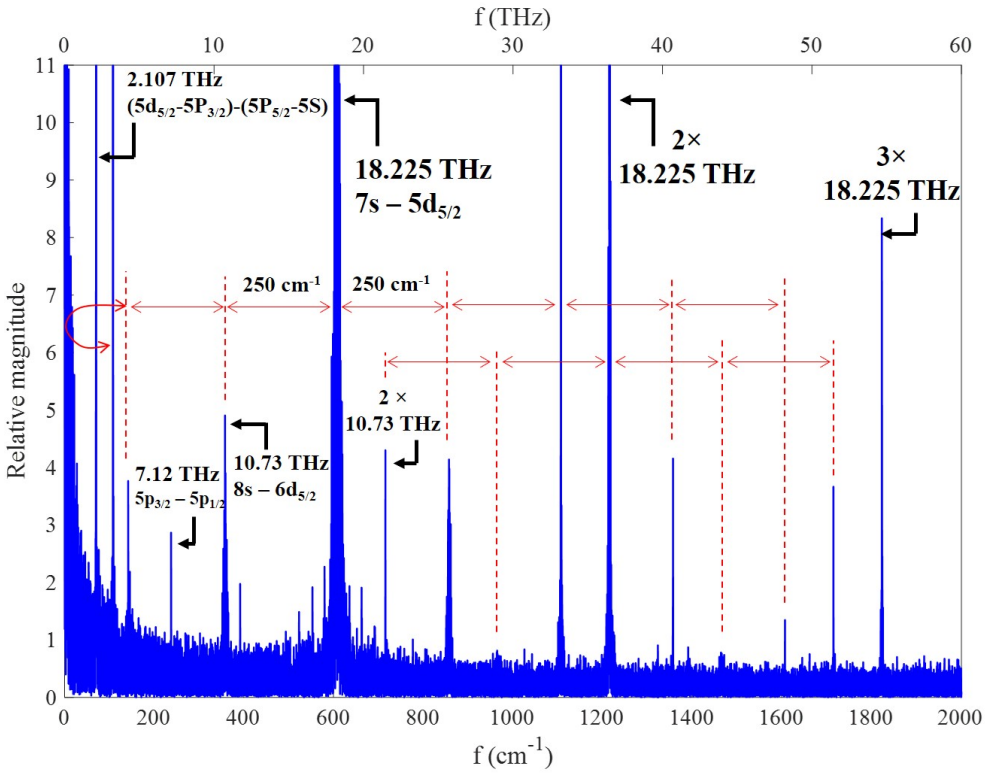

Figure 3.5: Zoomed-in view of the quantum beating spectrum. The peak at 2.11 THz corresponds to an energy difference of $(5d_{3/2}$-$5p_{3/2})$-$(5p_{3/2}$-$5s_{1/2})$ and the peak at 10.73 THz corresponds to the energy difference between $8s$ and $6d_{5/2}$ state. Also marked in the spectrum are the multiple harmonics of the 18.225 THz and 10.73 THz peaks, and the multiple replicas of difference between 18.225 THz peak and 10.73 THz peak symmetric to the 18.225 THz peak (see text and Equation 3.3).

quantum beating between $8s$ and $6d_{5/2}$ states, are successfully generated and observed in our experiment. The resolution of the DFT is 0.05 cm^{-1} (or 1.5 GHz) without zero padding. The uncertainties of NIST atomic states are 0.002 cm^{-1} (60 MHz) for $5p_{1/2}$ and $5p_{3/2}$ states, and 0.01 cm^{-1} (0.3 GHz) for all other states listed in Table 3.1. Notice that the discrepancy of $7s$ - $5d_{5/2}$ beating is only 0.02% from calculated value from NIST, and the discrepancy of $8s$ - $6d_{5/2}$, despite its low signal intensity, is only 1.20%.

Also visible in Figure 3.4 and listed in Table 3.1 are multiple harmonics of the 18.225 THz signal. Because the detector does not directly sample the fast oscillation of the beat signal but samples the signal for each pump-probe delay, these harmonics are not caused by the nonlinear responses of

the detector but reflect the nonlinearity of the atomic system. This indicates that the atoms are so strongly driven that the nonlinear susceptibility starts to play a role.

The peak at 10.73 THz (357.88 cm^{-1}) corresponds to the energy difference between $8s$ and $6d_{5/2}$ states. This is surprising because according to Figure 1.9, the energies of $8s$ and $6d$ states are outside of the bandwidth of the laser through two-photon excitation. Some coherent processes have to contribute to the population of $8s$ and $6d$ states in the system. Goldshlag [46] attempts to offer some explanations.

It is worth mentioning that peaks in category 3 imply that certain characteristic frequencies, in this case $\delta \approx 250.2\,\text{cm}^{-1}$, can be superimposed onto the quantum beating spectrum by appearing as overtones on both sides of a major strong peak. This is the major mechanism that enables us to observe molecular structures of long-range Rydberg molecules (LRRM) in quantum beating experiments, as we will discuss in detail in Section 3.2.

The data presented thus far were obtained using the high-accuracy scanning method introduced in Chapter 2. The high-speed method was also employed to survey a wide range of different experimental conditions in order to obtain an optimal condition for generating maximum quantum beating signals. Three major tested parameters are laser power, pulse chirp and crossing angle between the pump and probe beams. Some results are listed and discussed here.

Figure 3.6 shows $7s$-$5d$ quantum beating signal strength as a function of the pump-probe beam cross angles. The cross angle is defined in Figure 3.7. Notice maximum quantum beating happens not at zero angle (pump and probe beam completely overlapping) but at a negative cross angle. All other angles yield weaker quantum beating signals. Positive cross angles also yield weaker signals but the data were not recorded. This is consistent with the fact that parametric four-wave mixing requires proper angle alignment for phase-matching.

The high-speed scanning method was also employed to find optimal chirp of the laser for maximum quantum beating strength. Note that the change of the chirp is not implemented by external pulse shaping device at this stage (such as MIIPS), but by fine-tuning the distance between the compressor gratings in the laser. As a result, some chirps cannot be characterized by simple first orders, but contain complicated higher orders.

Table 3.1: Peaks identified on the rubidium quantum beating spectra compared with NIST data. Δ = ($7s$-$5d$)-($8s$-$6d$)=250.2 cm^{-1} (see Equation 3.4).

spectral peak identity	Measured location THz	cm^{-1}	NIST data THz	cm^{-1}	Discrepancy
$5s$-p-d	2.101	70.30	2.111	70.408	0.15%
($7s$-$5d$)-2×Δ	3.239	108.1			
($7s$-$5d$)-3×Δ (wraps)	4.252	141.9			
$5p_{3/2}$-$5p_{1/2}$	7.123	237.7	7.123	237.595	0.03%
8s-**6**$d_{5/2}$	10.726	357.88	10.715	357.426	0.13%
($7s$-$5d$)-($5s$-p-d)	16.116	537.72			
7s-**5**$d_{5/2}$	18.225	608.09	18.226	607.939	0.02%
$7s$-$5d_{3/2}$	18.312	610.99	18.314	610.901	0.02%
($7s$-$5d$)+($5s$-p-d)	20.321	678.03			
2×($8s$-$6d_{5/2}$)	21.464	716.16			
($7s$-$5d$)+1×Δ	25.726	858.37			
($7s$-$5d$)+2×Δ	33.210	1108.1			
2×($7s$-$5d_{5/2}$)	36.450	1216.2			
($7s$-$5d$)+3×Δ	40.702	1358.1			
2×($7s$-$5d_{5/2}$)+1×Δ	43.964	1466.9			
($7s$-$5d$)+4×Δ	48.194	1608.1			
2×($7s$-$5d_{5/2}$)+2×Δ	51.435	1716.2			
3×($7s$-$5d_{5/2}$)	54.675	1824.3			
4×($7s$-$5d_{5/2}$)	72.889	2432.0			

Figures 3.8, 3.9 and 3.10 show the pulse analysis using frequency resolved optical gating (FROG) for three different chirps of the pulses. They include the directly measured spectrogram (FROG trace), retrieved spectrogram (retrieved Fourier transform), temporal amplitude and phase and spectral amplitude and phase. From Figure 3.8 to 3.9 to 3.10 the laser pulse becomes more and more negatively chirped as a result of tuning the laser compressor grating in one direction.

The change of $7s$-$5d$ quantum beating signal strength as the laser pulse becomes more negatively chirped is shown in Figure 3.11. Quantum beating signal strength is plotted as a function of pulse width, autocorrelation width and time-bandwidth (TBW) product. The pulses presented in Figures 3.8, 3.9 and 3.10 are also marked on the plot. The compressor is not capable of introducing a perfectly linear chirp, but as the grating is tuned in one direction, more negative element of the chirp is introduced. From Figure

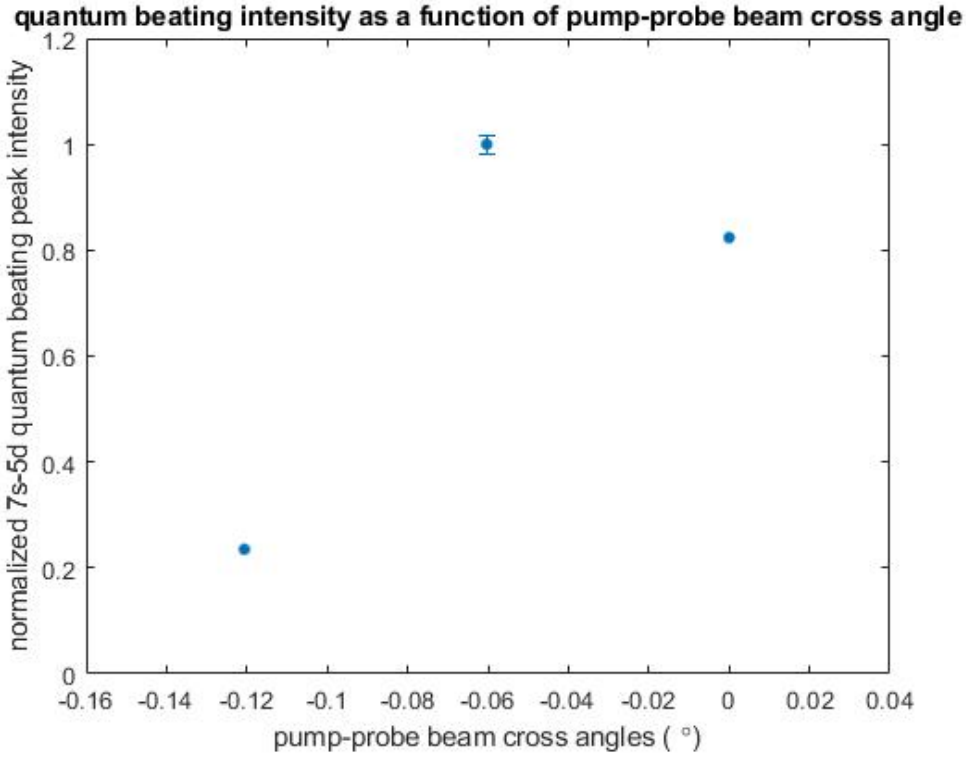

Figure 3.6: $7s$-$5d$ quantum beating signal intensity as a function of the pump-probe beam cross angle, obtained by utilizing high-speed scanning method. Only the error bar for pump-probe cross angle of -0.06° is marked (others not recorded). The height of the error bar represents one standard deviation computed from three data samples. The cross angle is defined from the probe beam to the pump beam (illustrated in Figure 3.7). On a plane perpendicular to the probe beam, positive cross angle implies the pump beam is on the right side of the probe beam and vice versa. Notice that maximum quantum beating happens at a negative cross angle. Positive cross angles yield weaker quantum beating signals but the data were not recorded.

3.11 we see that as more negative chirp is introduced by the compressor, the actual laser pulse keeps extending wider in time (autocorrelation width) monotonically, but the measured pulse will first become larger, hitting a maximum value, then become smaller. This behavior can also be observed on the time-bandwidth (TBW) product plot; the TBW product first becomes larger then smaller. We see that negative chirp does help to increase the quantum beating signal strength, but there is a limit. The quantum beating signal tends to be the largest when the laser pulse has a negative chirp and also a maximum TBW product, or the maximum measured pulse width.

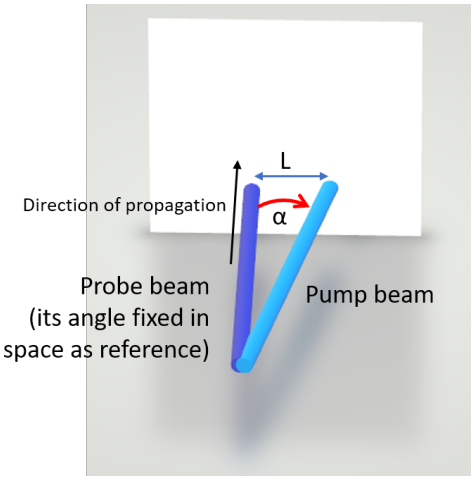

Figure 3.7: Illustration of how pump-probe cross angle is defined in Figure 3.6. Both beams are parallel to the ground. The cross angle is defined by the probe beam and pump beam. Positive cross angle means the pump beam is on the right side of the probe beam on a plane perpendicular to the probe beam.

Previous study shows that population transfer to the upper levels is more efficient with positively chirped pulses [51], which undesirably reduces the strength of quantum beats because the PFWM process also relies on the population of ground state. More discussions of the chirp's influence on the quantum beating strength can be found in [40, 41].

3.2 Long-range Rydberg Molecules

In Section 3.1 we mentioned that on the quantum beating spectrum, overtones of certain frequency spacing appear on both sides of a dominant peak. In that case, the overtones of 250 cm^{-1} (frequency difference between $7s$-$5d_{5/2}$ and $8s$-$6d_{5/2}$ beating peaks) appear on both sides of the $7s$-$5d_{5/2}$ peak. We found this phenomenon occurring with other frequency spacings around other center peaks. Analysis points out that these newly discovered frequency spacings can be attributed to the molecular structure of the long-range Rydberg molecules associated with the atomic energy levels that contribute to the major quantum beating peak at the center. The observation and analysis are detailed in this section.

Figure 3.12 shows a zoom-in of the quantum beat spectrum of the region

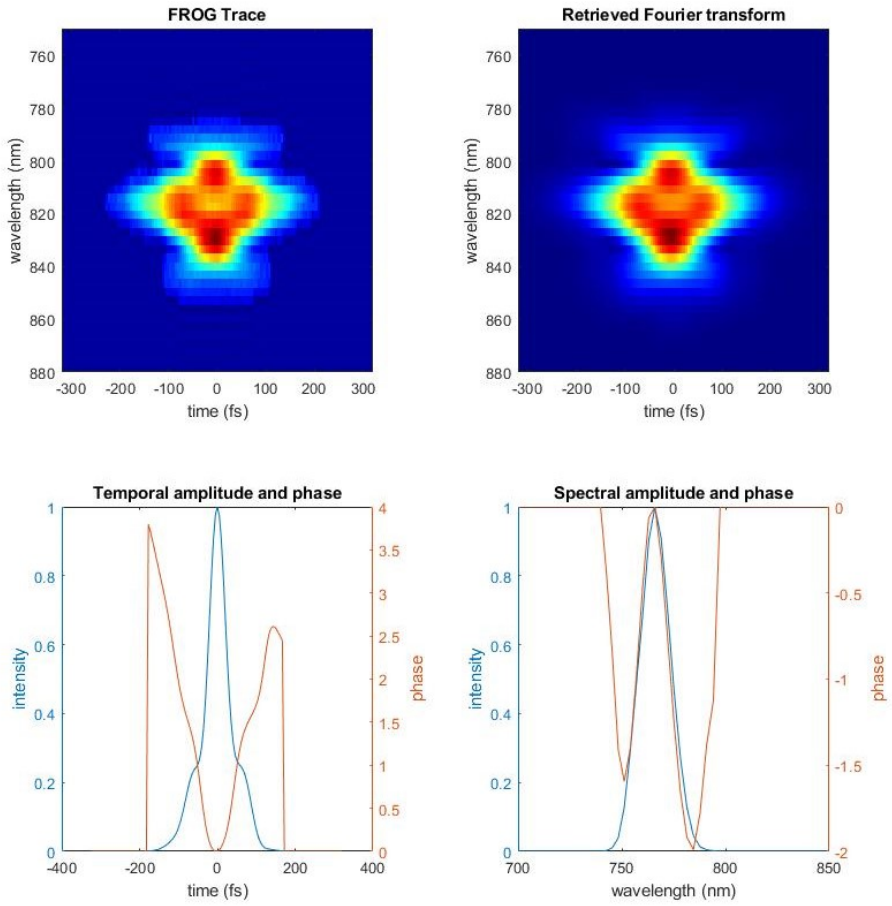

Figure 3.8: FROG analysis of lasers pulses, case 1.

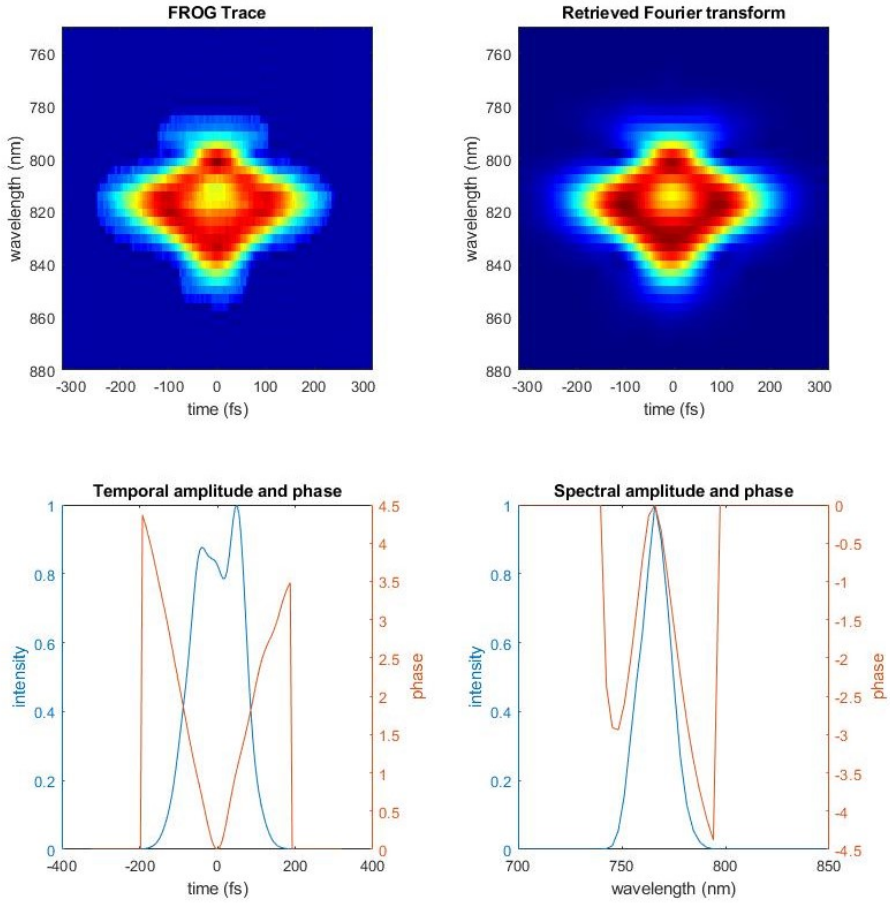

Figure 3.9: FROG analysis of lasers pulses, case 2.

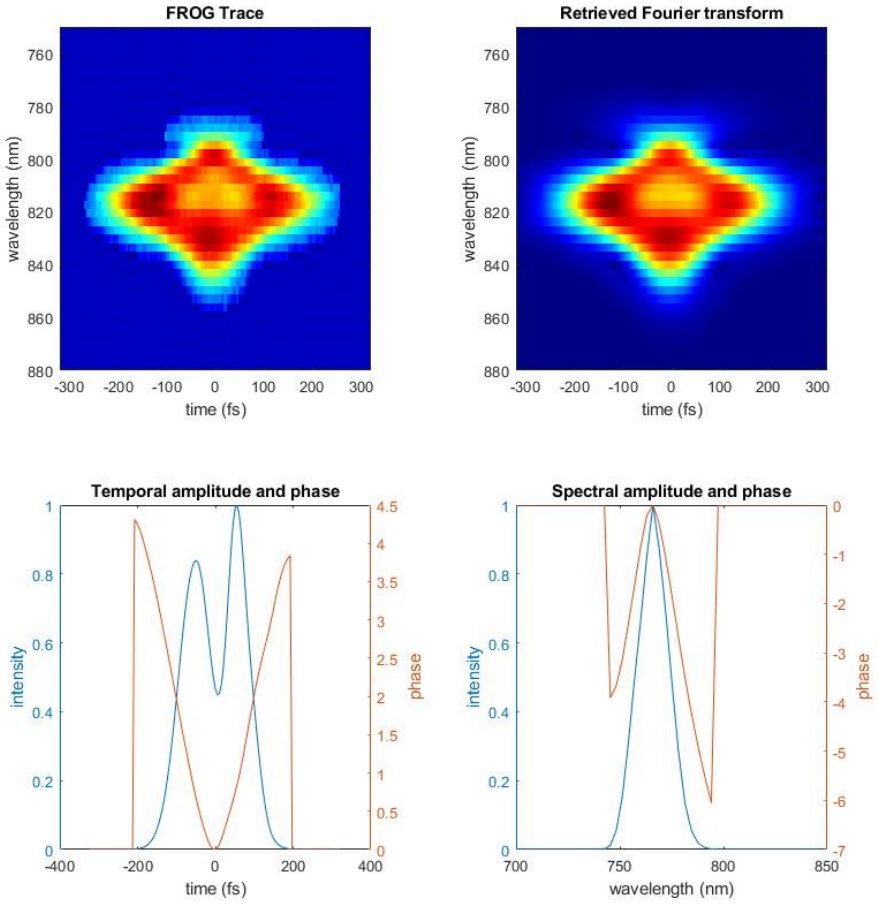

Figure 3.10: FROG analysis of lasers pulses, case 3.

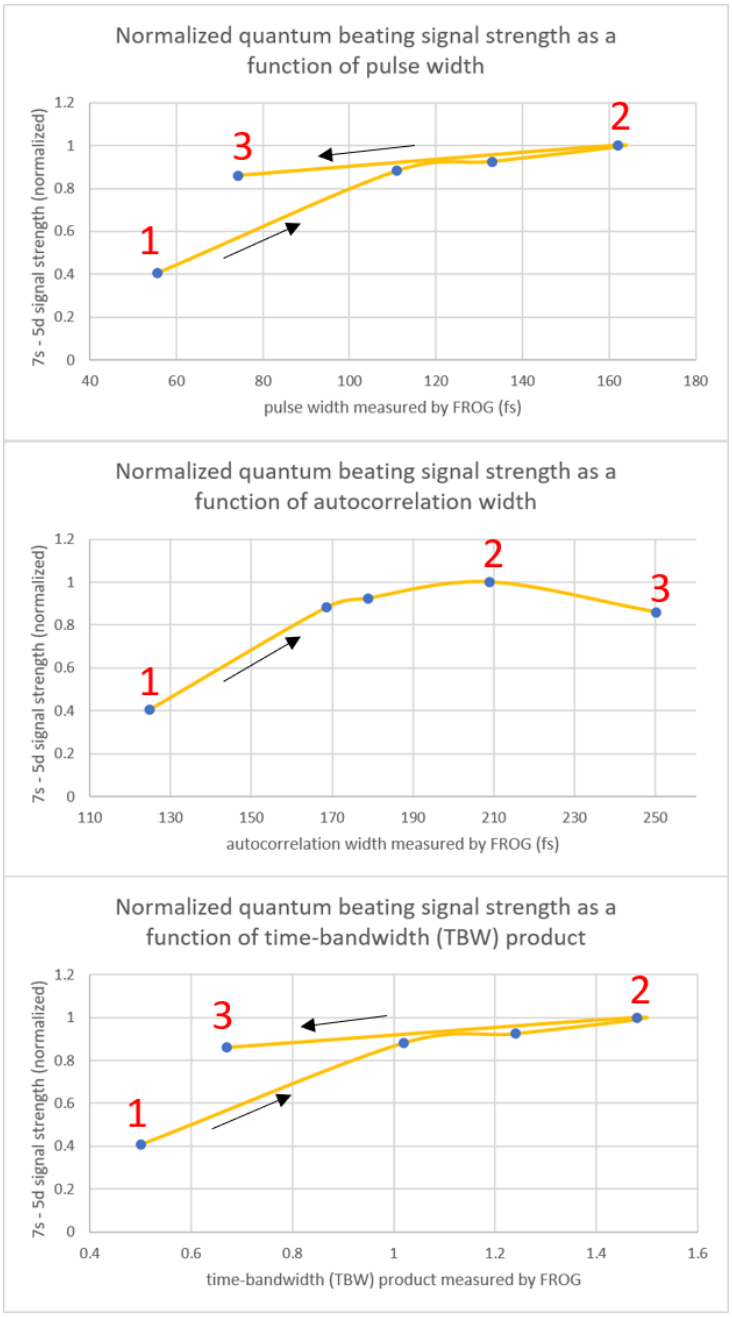

Figure 3.11: Normalized $7s$-$5d$ quantum beating signal strength as a function of various laser pulse parameters measured by FROG. **top**: pulse width, **middle**: pulse autocorrelation width, **bottom**: time-bandwidth (TBW) product. Note the arrows point to the direction when the chirp becomes more negative as a result of tuning laser compressor gratings. The numbers (1,2,3) marked on the traces refer to the cases presented in Figures 3.8, 3.9 and 3.10.

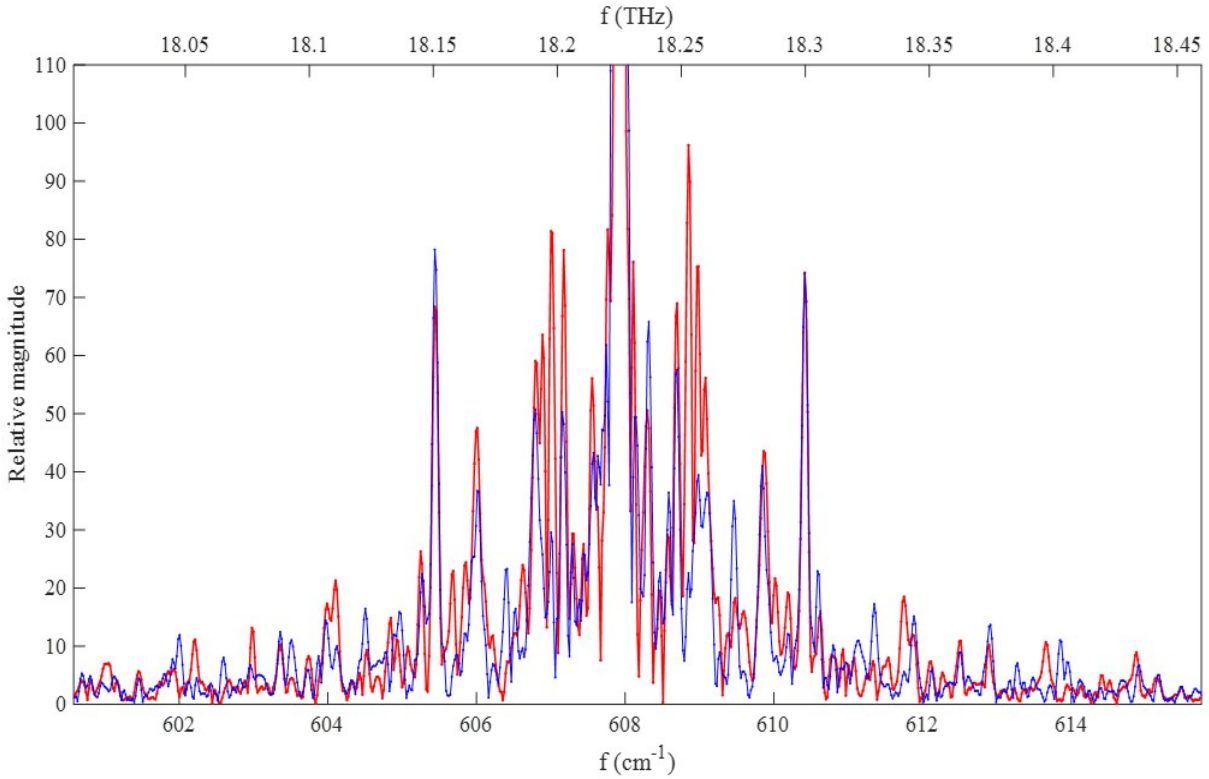

Figure 3.12: Two traces of the 18.225 THz quantum beating peak showing reproducibility of the spectrum.

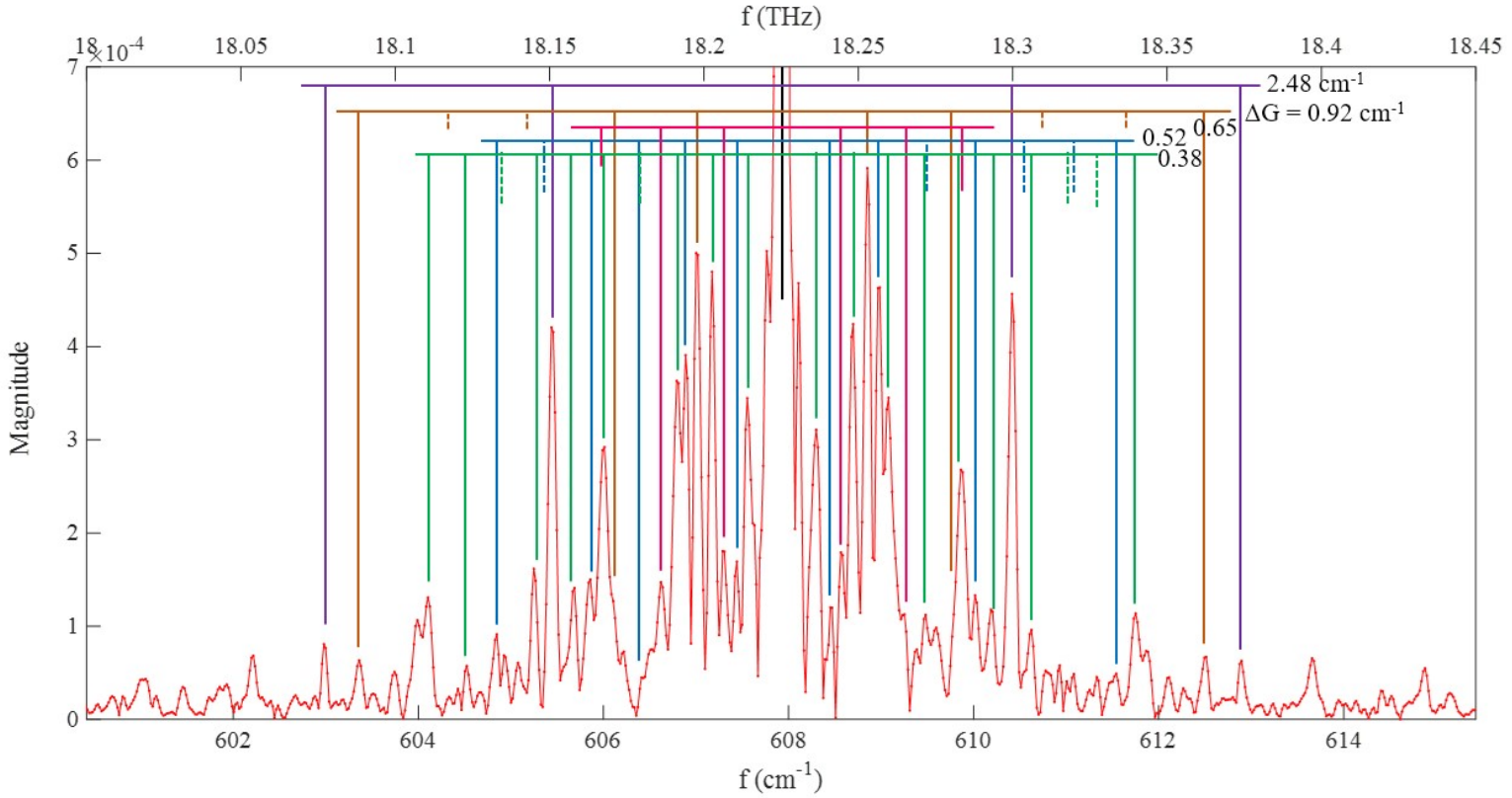

Figure 3.13: Zoomed-in view of the quantum beating spectrum around the 18.225 THz ($7s$-$5d_{5/2}$) peak. Lines of the same color mark a series of peaks that are equally spaced by ΔG. Five series are marked with their ΔGs labeled.

towards the bottom of the strong 18.225 THz peak, where many structures can be spotted on the both sides of the 18.225 THz peak. The relative magnitudes of these side peaks are one order of magnitude smaller than the 18.255 THz peak but still distinguishable from the noise level.

Notice that two traces are shown in Figure 3.12 (red and blue). The two traces of data were obtained from two different sets of data taken at two different dates, but with the same experimental conditions, including the same laser characteristics such as equal laser power (150 μJ per pump and probe pulse, measured after oven) and negative chirp. The oven temperature (cold finger) is set at 170 °C, corresponding to a gas number density of 2.5×10^{14} cm^{-3}. We can see that the **locations** of the majority of the peaks are highly reproducible, within at most three pixels' error. The relative magnitudes of some but not all of the peaks are reproducible. In our discussions here, the reproducibility of the peaks' relative magnitude is not as important as that of the **location**, which is determined by the molecular structure we are interested in. Lastly, it is worth mentioning that more than two sets of data were taken to confirm the reproducibilities of the peaks' locations, but only two traces are shown in Figure 3.12 for clarity.

As mentioned in Section 3.1, according to Equation 3.1, the resolution of the DFT without zero padding (real resolution) is 0.05 cm^{-1} (1.5 GHz). However, the spectrum in Figure 3.13 was obtained by zero-padding the data to twice the next power of 2 of the total number of data points in order to improve the "smoothness" of the spectrum. The zero padding elevates the spectroscopic resolution to 0.019 cm^{-1} (0.57 GHz) in appearance on the spectrum, even though it is not a real resolution which is determined only by the sampling frequency and the number of samples taken without zero padding. The difference between the real resolution and the resolution appearing on the spectrum as a result of zero padding is summarized in Table 3.2.

Figure 3.14 shows a Lorentzian fit (homogeneous broadening) for the strong atomic quantum beating peak at 18.225 THz. The linewidth fit yields a full width at half maximum (FWHM) of 3 GHz. A similar process was carried out for various numbers of peaks, including those peaks shown in Figure 3.13 and Figure 3.16. The FWHMs of these peaks vary slightly but are all within 2.5 to 5.5 GHz range, which is one order of magnitude larger than the apparent resolution of the spectrum (with zero padding) and at least twice as large as the real resolution (without zero padding).

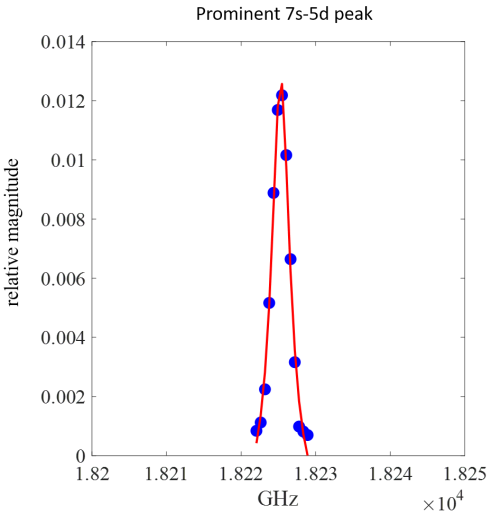

Figure 3.14: Lorentzian linefit for the prominent peak at $7s$-$5d$ shows a linewidth of 3 GHz.

Table 3.2: Resolutions of the spectrum.

scanning range	number of raw samples	real resolution without zero padding	apparent resolution with zero padding[1]
100 mm	197282	0.05 cm^{-1}(1.5 GHz)	0.019 cm^{-1} (0.57 GHz)

[1]padded to 2 times of the next power of 2 of the original number of samples

As will be shown in Section 3.2.2, symmetric to the center frequency of 18.255 THz, multiple series of overtones appear on both sides of the 18.255 THz peak. All major peaks in Figure 3.12 belong to one of these overtone series. Further analysis shows that the fundamental frequencies of these overtones can be derived as different vibrational modes of a low-order anharmonic oscillator, indicating diatomic molecular structure.

A similar phenomenon can be observed in the vicinity of the $8s$-$6d_{5/2}$ peak on the quantum beating spectrum and the frequencies of the overtones also fit into vibrational modes of a diatomic molecule, although the derived vibrational constants are different from the $7s$-$5d_{5/2}$ case. The next section discusses the molecular structure in the $8s$-$6d_{5/2}$ case and then the $7s$-$5d_{5/2}$ case.

3.2.1 LRRM Structure Near $8s$-$6d_{5/2}$ Difference Frequency

Figure 3.15 shows two traces of the spectra near the $8s$-$6d_{5/2}$ quantum beating peak under the same experimental condition as those in Figure 3.13. Again, the positions of most of the peaks in the spectrum are highly reproducible.

Careful examination of the peaks reveals that distances between certain peaks are equal to each other. There are multiple series of equal distances between the peaks. They are labeled in Figure 3.16. Each color of the straight lines in the figure designates a series of equidistant peaks. Relative to a center peak at around 10.726 THz, each series of peaks can be regarded as overtones of a fundamental frequency, which is the distance between two adjacent peaks belonging to the same series. In the figure, these fundamental frequencies of the overtones are marked next to each series in wavenumbers (cm^{-1}).

As shown in Figure 3.16, out of the total number of 61 peaks of significant magnitude on the spectrum, 48 peaks are identified to belong to one of the 8 series of overtones. For reasons that will become apparent shortly, the 8 series of peaks are divided into two groups. In Figure 3.16, one group encompasses the peaks that are marked with lines and labels at the top of the figure (designated as **top series**) and the other group encampasses peaks at the bottom of the figure (designated as **bottom series**).

Next, for each group of the series, we try to assign an integer index number

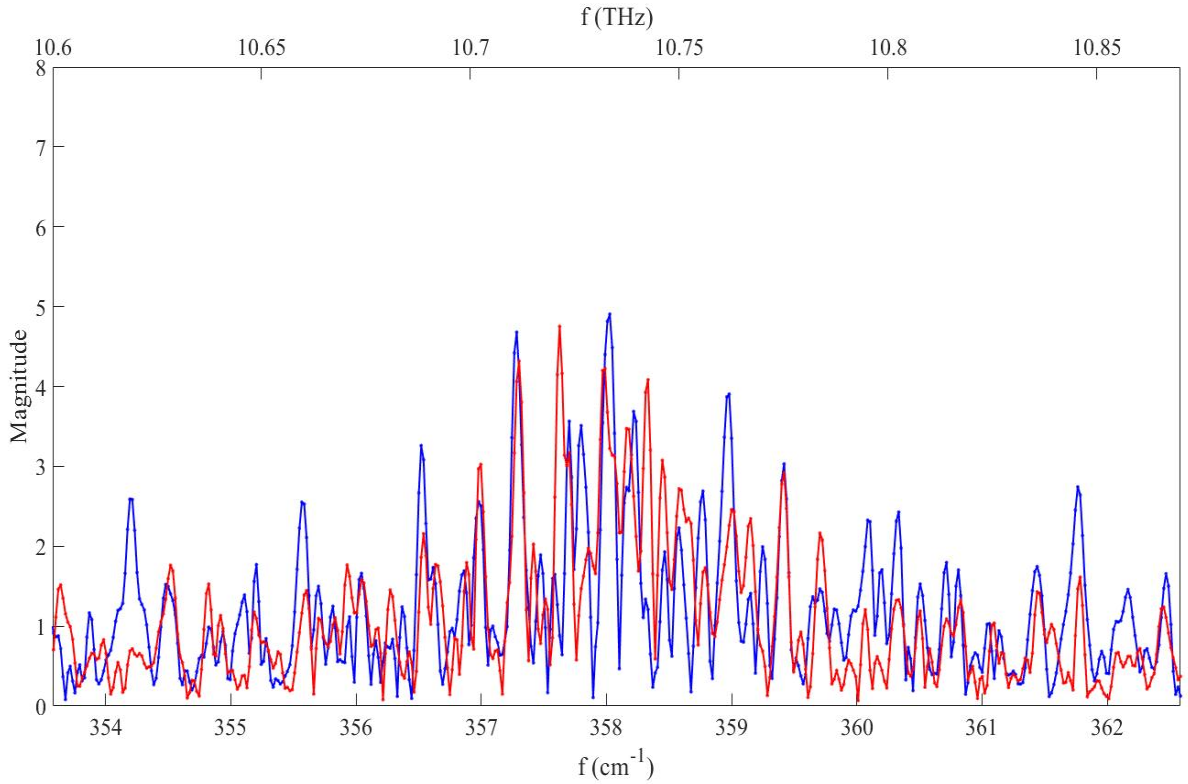

Figure 3.15: Two traces of the $8s$-$6d_{5/2}$ quantum beating peaks around 10.73 THz showing reproducibility of the spectrum.

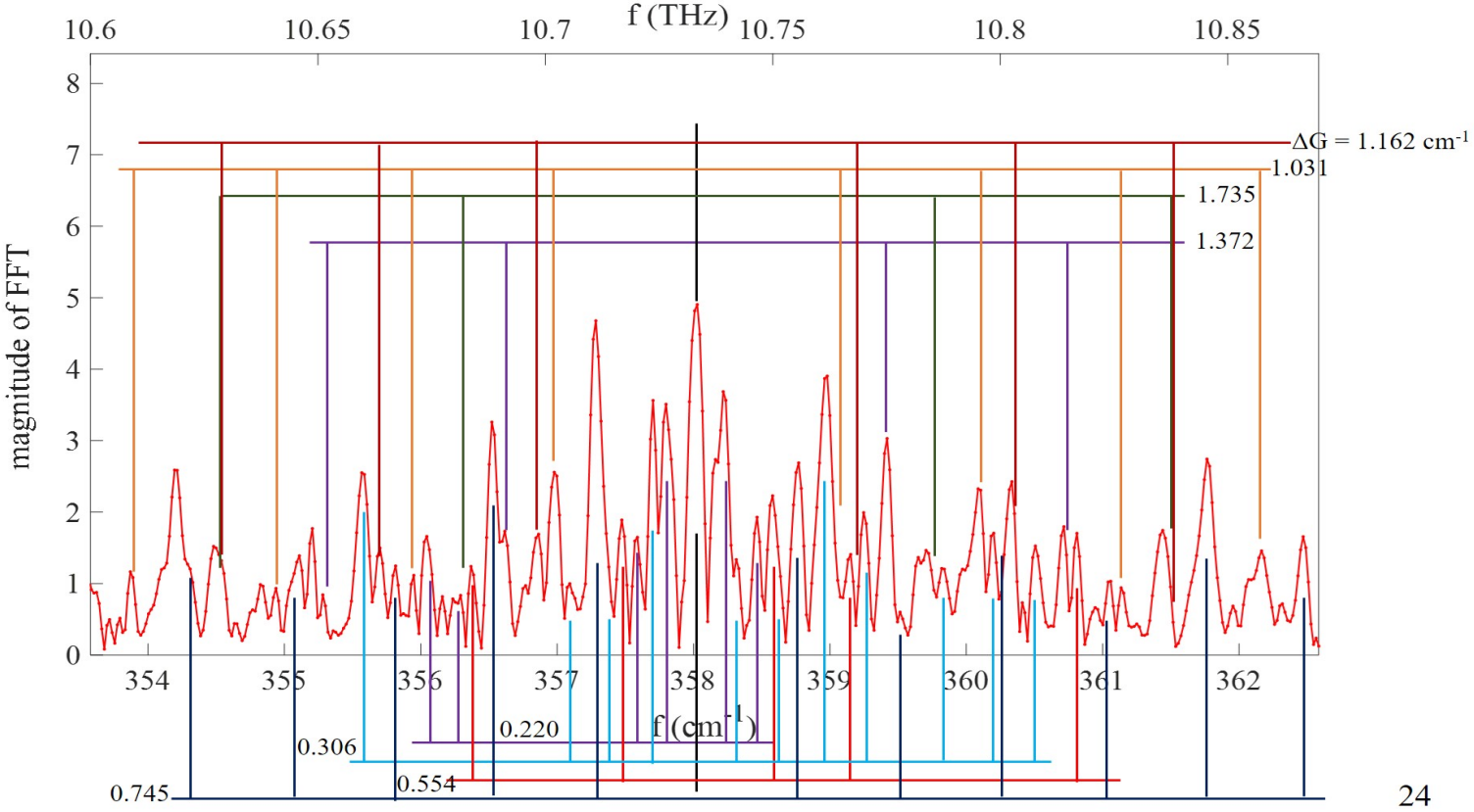

Figure 3.16: Zoomed-in view of the quantum beating spectrum around the 10.73 THz ($8s$-$6d_{5/2}$) peak. Lines of the same color mark a series of peaks that are equally spaced by ΔG. In total, eight series are marked with their ΔGs labeled.

v to each series within the group, i.e. for the **top series** assigning $v = 1$ to the series with the largest energy spacing ΔG = 1.735 cm^{-1}, assigning $v = 2$ to the series with the next largest spacing ΔG = 1.372 cm^{-1}, and so on. If we plot the energy spacing ΔG (or the fundamental frequency of the overtones) as a function of the index number v, we find a quadratic relation (or a higher order polynomial) between the two variables, as shown on the left of Figure 3.17 (**left: top series**). Similar assignment can be done to the **bottom series** of the overtones, and the relation between ΔG and integer number v is plotted on the right of Figure 3.17 (**right: bottom series**), which is approximately linear.

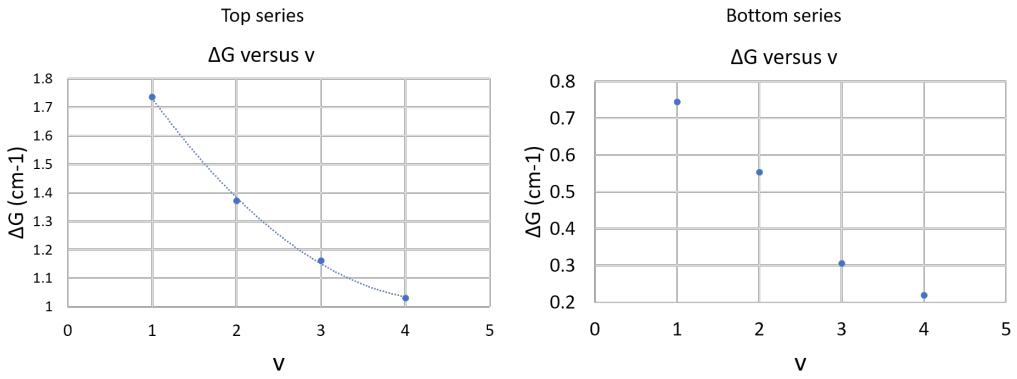

Figure 3.17: Equal energy spacing (fundamental frequency of overtones) ΔG as a function of the index number v (the vibrational quantum number) for both **left: top series** and **right: bottom series** derived from the $8s$-$6d_{5/2}$ quantum beating spectrum.

Recall that in molecular spectroscopy, under the Born-Oppenheimer approximation, the vibrational energy terms of a molecule's electronic potential well can be derived from an anharmonic oscillator to be [52]

$$G(v) = \omega_e(v + \frac{1}{2}) - \omega_e x_e(v + \frac{1}{2})^2 + \omega_e y_e(v + \frac{1}{2})^3 + \omega_e z_e(v + \frac{1}{2})^4 ... \quad (3.5)$$

where $v = 0,\ 1,\ 2,\ ...$ is the vibrational quantum number designating the index of the corresponding vibrational level counted from the bottom of the potential well, and ω_e, x_e and y_e are vibrational constants determined by the shape of the potential well. Note that Equation 3.5 describes the vibrational term energy to only the fourth order of the vibrational quantum number v. Higher order terms can be included for more accurate approximations but for our analysis four orders are sufficient.

Keeping only the first and second order terms in Equation 3.5 and writing the differences between two adjacent vibrational energy terms yields the energy spacing between the adjacent vibrational energy levels

$$\Delta G(v) = (\omega_e - 2\omega_e x_e) - 2\omega_e x_e v \tag{3.6}$$

which is a linear function to the vibrational quantum number v and $v = 1$, 2, 3, ... There is no v=0 in the ΔG expression as $G(v = 0)$ serve as the subtrahend of $G(v = 1)$.

Keeping the first, second, third and fourth order terms in Equation 3.5 and writing the differences between two adjacent vibrational energy terms yields the energy spacing between the adjacent vibrational energy levels

$$\Delta G(v) = (\omega_e - 2\omega_e x_e + \frac{13}{4}\omega_e y_e) - (2\omega_e x_e - 6\omega_e y_e - \omega_e z_e)v + 3\omega_e y_e v^2 + 4\omega_e z_e v^3 \tag{3.7}$$

which is a cubic function to the vibrational quantum number v and again v starts with 1.

Assuming that the energy spacings (or the fundamental frequencies of overtones) in Figure 3.17 are actually the energy spacings between adjacent vibrational energy levels in the electronic potential wells of a long-range Rydberg molecule associated with either the $8s$ or $6d_{5/2}$ state, then the top and bottom series belong to two different electronic potential wells. The top series represents the well where the spacing between adjacent vibrational energy levels is described as at least a quadratic function to vibrational quantum number v (Equation 3.7), while the bottom series represents the well where the spacing is described as a linear function of v (Equation 3.6, possibly because the coefficient of the third and higher order terms in Equation 3.5 $\omega_e y_e$ are negligible in the bottom series quantum well).

On the surface it seems that using a quadratic function is sufficient to fit the relation between ΔG and v for the top series (Figure 3.17, left). The fitting is indeed shown in Figure 3.18 (red trace). This yields vibrational constants up to the third order

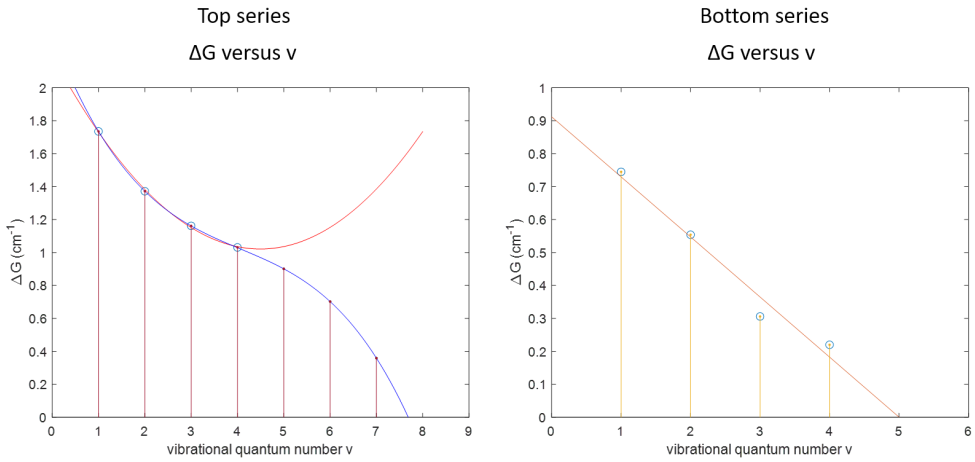

Figure 3.18: Fitting ΔG as a function of the vibrational quantum number v, for both **left: top series** and **right: bottom series**. Open circles designate the data points directly observed from the quantum beat spectrum while dots on the trace designate data points not directly observed but extrapolated from the fitted function. Notice that the top series is fitted by both a quadratic (red trace) and cubic function (blue trace). However, the quadratic function extrapolates an infinite number of vibrational energy levels whose spacing becomes monotonically larger at v larger than 5, leading to an unphysical solution of infinite well depth.

$$\begin{aligned} \omega_{e_1} &= 2.772 \text{ cm}^{-1} \\ \omega_{e_1} x_{e_1} &= 0.319 \text{ cm}^{-1} \\ \omega_{e_1} y_{e_1} &= 0.019 \text{ cm}^{-1} \end{aligned} \tag{3.8}$$

Even though only four energy spacings between vibrational levels were observed on Figure 3.18 (left), more ΔG values for other vibrational quantum numbers within the well can be extrapolated using the fitted function. This shows us that using only a quadratic function to fit ΔG versus v is not sufficient because ΔG will become monotonically larger as v increases beyond 5, indicating an infinite number of vibrational energy levels within an infinitely deep potential well.

Instead, using the cubic function to fit the data circumvents this problem. Fitting the data of the top series in Figure 3.17 to Equation 3.7 yields the

vibrational constants for its quantum well

$$\begin{aligned} \omega_{e_1} &= 3.19 \text{ cm}^{-1} \\ \omega_{e_1} x_{e_1} &= 0.51 \text{ cm}^{-1} \\ \omega_{e_1} y_{e_1} &= 0.05 \text{ cm}^{-1} \\ \omega_{e_1} z_{e_1} &= -0.003 \text{ cm}^{-1} \end{aligned} \tag{3.9}$$

The fitted cubic function is shown in Figure 3.18 (left) as the blue trace. We see now that the energy spacing ΔG decreases monotonically as v becomes larger until it reaches zero, indicating a limited number of vibrational energy levels within the cell. The extrapolated ΔGs for not observed v are marked as dots in Figure 3.18, from which we now see that there are in total 8 vibrational energy levels within the cell (7 energy spacings between adjacent levels, 4 of the them directly observed and 3 extrapolated).

Comparing the vibrational constants fitted from a quadratic function (Equation 3.8) with those fitted from a cubic function (Equation 3.9) we see the results are actually very similar. Equation 3.9 added a fourth order term that is negligibly small (-0.003 cm^{-1}), 8 times smaller than the apparent resolution of the spectrum of 0.019 cm^{-1}, even though the existence of this term is necessary to guarantee the potential well has a definite depth. For the remaining three orders of the vibrational constants, Equation 3.8 and Equation 3.9 yield remarkably close values. Further examination shows the highest order constant $\omega_{e_1} y_{e_1}$ in Equation 3.8 is almost the same value as the apparent resolution of the spectrum, indicating a higher order term $\omega_{e_1} z_{e_1}$ might need to be added for a better fitting.

The bottom series does not have the ambiguity in choosing the order of fitting function as a monotonically decreasing linear function is guaranteed to produce a limited number of levels within a well. Fitting the data of the bottom series in Figure 3.17 to Equation 3.6, yields the vibrational constants for the other quantum well

$$\begin{aligned} \omega_{e_2} &= 1.094 \text{ cm}^{-1} \\ \omega_{e_2} x_{e_2} &= 0.091 \text{ cm}^{-1} \end{aligned} \tag{3.10}$$

These constants are smaller than those of the first well.

Now we are able to derive the dissociation energies and potential energy curves for these quantum wells. Figure 3.19 shows an example of such PEC.

The work that needs to be done in order to dissociate a molecule is called dissociation energy D_0, which is the energy difference between the lowest vibrational level and the atomic asymptote. It is apparent from Figure 3.19 that D_0 is equal to the sum of all the vibrational energy spacing within the potential well, i.e.

$$D_0 = \sum_v \Delta G_v \tag{3.11}$$

where v = 1, 2, ...

Thus, D_0 is also the "area" under the ΔG curve in Figure 3.18 by summing up all the ΔG values that are positive. This yields D_0 for the two potential wells to be

$$\begin{aligned} D_{0-8s6d-well1} &= 7.26 \text{ cm}^{-1} \\ D_{0-8s6d-well2} &= 1.73 \text{ cm}^{-1} \end{aligned} \tag{3.12}$$

D_0 is the energy difference from the lowest vibrational level to the atomic asymptote. D_e, on the other hand, designates the energy difference from the bottom of the potential curve of the well to the atomic asymptote. D_e is D_0 plus the vibrational energy of the lowest vibrational level, G(0), also called zero-point energy,

$$D_e = D_0 + \text{G}(0) = D_0 + \frac{1}{2}\omega_e - \frac{1}{4}\omega_e x_e + \frac{1}{8}\omega_e y_e + \frac{1}{16}\omega_e z_e \tag{3.13}$$

D_e, or the dissociation energy referred to the electronic potential minimum, for the two potential wells are found to be

$$\begin{aligned} D_{e-8s6d-well1} &= 8.99 \text{ cm}^{-1} \\ D_{e-8s6d-well2} &= 1.82 \text{ cm}^{-1} \end{aligned} \tag{3.14}$$

Potential energy curves for the wells can be obtained from the vibrational constants and dissociation energies derived above. An analytical form of such potential that accounts for all vibrational levels within the well is proposed by Morse [53]

$$U(r - r_e) = D_e(1 - e^{-\beta(r-r_e)})^2 \tag{3.15}$$

where r is the internuclear distance, r_e is the internuclear distance at equi-

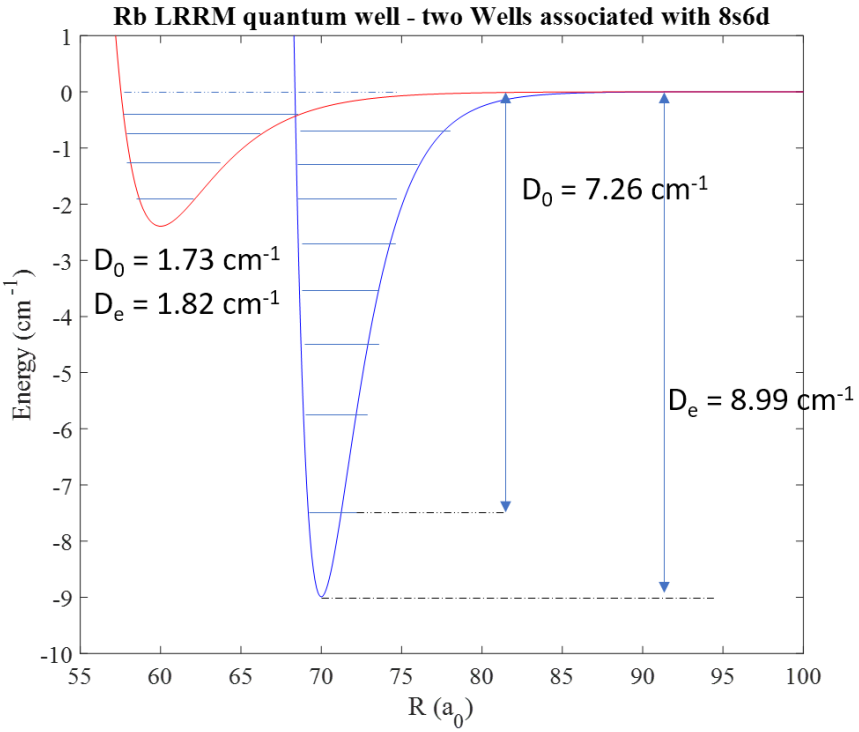

Figure 3.19: The derived potential energy curves for the LRRM associated with $8s$ and $6d$ atomic energy level asymptote. Two wells were computed using the vibrational constants derived from the two series of equal spacing overtones from the quantum beating spectrum. The potential curves are modeled as a Morse potential and the internuclear distances at equilibrium are chosen according to the scaling law. The dissociation energies of the wells are marked on the PEC. A number of supported vibrational energy levels are drawn within each well but their positions are only drawn approximately.

librium (bottom of the well), and the constant β will be determined shortly.

Given the potential, Morse derived the vibrational term energies to be

$$G(v) = \beta\sqrt{\frac{D_e h}{2\pi^2 c\mu}}(v+\frac{1}{2}) - \frac{h\beta^2}{c8\pi^2\mu}(v+\frac{1}{2})^2 \tag{3.16}$$

which writes out only the first two orders of $(v+\frac{1}{2})$. μ is the reduced mass of the molecule, c is the speed of light and h is Planck's constant. Comparing Equation 3.16 with Equation 3.5 and equating the coefficients of $(v+\frac{1}{2})$, β can be written as a function of the dissociation energy D_e and the first order vibrational constant ω_e

$$\beta = \sqrt{\frac{2\pi^2 c\mu}{D_e h}}\omega_e = 1.2177\times10^7\omega_e\sqrt{\frac{\mu_A}{D_e}}\ \mathrm{cm}^{-1} \tag{3.17}$$

where both ω_e and D_e are in cm^{-1} units and μ_A is reduced mass in atomic mass units.

Utilizing the values of D_e in Equation 3.14 and ω_e in Equation 3.9 and 3.10, we are able to compute the electronic potential curves of the two wells using Morse's model, as shown in Figure 3.19. Also shown are the supported vibrational levels within each well, and the corresponding dissociation (or binding) energies D_0 and D_e. The equilibrium internuclear distances R_e are approximated using the scaling law ($\mathrm{R}_e \propto n^2$) from known wells at higher principal quantum numbers. The two wells are placed next to each other on the PEC, assuming the deeper well is the outermost well. This is a reasonable assumption considering both the theory and experimental observations. Also assumed is that there is no interaction between the curves of the two wells, while in reality the two wells may merge near the atomic asymptote. From Figure 3.18 (right) we can see that for the shallower well, there are some deviations from the linear relation between ΔG and v at high v, which might be caused by the interaction between the two wells near the atomic asymptote.

Now we want to compare our results with the published experimental results. Unfortunately, there are no available data on the exact LRRMs associated with the $8s$ and $6d_{5/2}$ Rydberg states. The closest available PEC is the one associated with the $11p$ state [6], which is shown in Figure 3.20, from which the first order vibrational constant is extracted to be 1.05 cm^{-1}. This

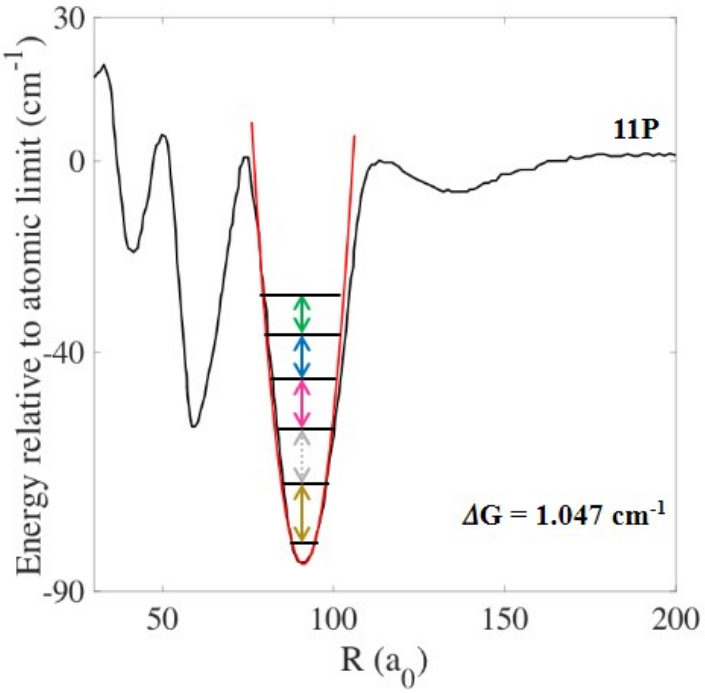

Figure 3.20: The potential energy curve of the LRRM associated with the $11p$ state in Rb [6]. The first order vibrational constant is fitted to be 1.05 cm^{-1}.

value is on the same order of magnitude as those values in Equation 3.9 and 3.10 we extracted. On the other hand, Figure 3.20's PEC is for an LRRM associated with a P-state atom, while ours are associated with either S or D state. There are no PEC data available for the S and D states at these low principal quantum numbers close to ours. The lowest D state published is $n = 24$ and the lowest S state is $n = 34$. In both cases only the two lowest vibrational levels $v = 0, 1$ are observed in their corresponding wells. Even so, the binding energy data (or dissociation energy) become available from $v = 0$. Theoretically, the dissociation energies (or binding energies) of these quantum wells get shallower as n^{-6}. So collecting D_0 from published data and extrapolating the binding energies to low principal quantum numbers we are able to compare them with our observation. This is shown in Figure 3.21.

The binding energies for molecules associated with atomic nS levels were fitted and extrapolated from Bendkowsky *et al.*'s data of $n = 34-40$ [8] while the nD ones were fitted from Anderson *et al.*'s data of similar principal quantum numbers [14]. The extrapolated binding energies at principal quantum

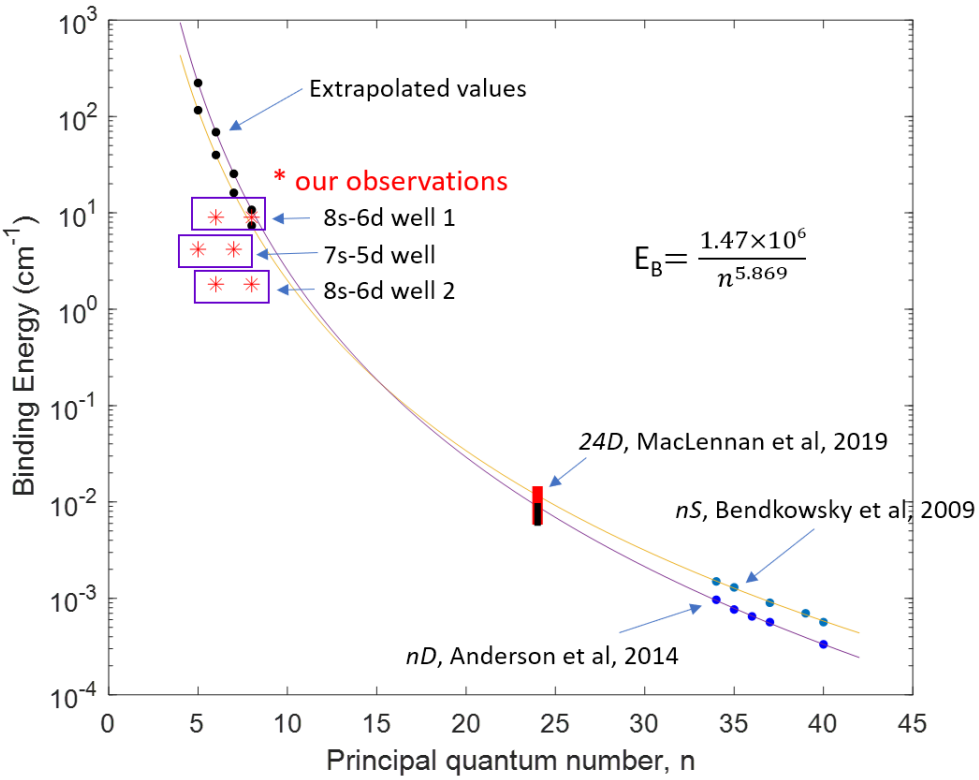

Figure 3.21: The binding energy of long-range Rb_2's potential wells versus the principal quantum number n of the involving Rydberg atom. The relation was fitted from Bendkowsky *et al*'s data of $n = 34 - 40$S [8] and Anderson *et al*'s data of $n = 34 - 40$D [14](blue dots). MacLennan *et al.*'s data of 24D [30] are also marked on the figure as the thick red and black bars to show the extent of accuracy of the fitting. The red and black bar designate the range of binding energies measured for different spin couplings all associated with the atomic 24D state (red for J=3/2 and black for J=5/2). The extrapolated binding energies associated with $n = 5 - 8$ S and D states are marked as black dots and are compared with values measured from our experiment marked as red asterisks. The comparison shows that our measured values are smaller than the binding energies predicted by the scaling curve but still quite close, considering the scaling law may deviate at these low principal quantum numbers of our interest.

numbers $n = 5-8$ are marked as black dots on the figure and compared with the red asterisks that mark the binding energies of our observations. Another set of data from MacLennan *et al.* [30] for $24D$ is also marked on the trace for comparison. We see that the binding energies derived from our quantum wells are close to the extrapolated values, within an order of magnitude. The comparison also shows that, except for the binding energy derived from the well 1 from the $8s$-$6d$ quantum beat and assigned to the PEC associated with $8s$ atomic state, the binding energies derived from observation are smaller than those extrapolated from fitting. The binding energy associated with $7p$ state from Bellos and Carollo's studies [11, 29], although not associated with s or d state, being slightly over 100 cm^{-1}, is also larger than our observations. This might be due to three reasons. Firstly, it might be due to the deviation from theory at low principal quantum numbers for those associated with s and d states. Secondly, the oscillatory shape of the PEC produces multiple potential wells, some of which are significantly shallower than the others. Thirdly, deriving dissociation energy of a quantum well from a limited number of observed vibrational energy spacings is a simplification. Towards the top of a potential well, the influence of dissociation limit and the interaction between nearby wells make the shape of the PEC more irregular and deviate more from an approximation of limited orders that work better at the bottom of the well. In any case, the dissociation energy derived from our observed vibrational energy level spacings appears to be an underestimate, but still within one order of magnitude of those of the p state and those extrapolated from higher order s and d states.

In summary, we are able to derive the vibrational constants, dissociation energies, and PECs of two LRRM potential wells by analyzing the sidebands of the $8s$-$6d$ atomic quantum beat on the spectrum. The observations and derivations are compared and found to be remarkably similar to those of previously published studies.

As mentioned earlier, similar sidebands of overtones can also be observed around the $7s$-$5d_{5/2}$ atomic quantum beating peak. Similar analysis is conducted and reveals additional long-range molecular structures associated with the $7s$ and $5d_{5/2}$ atomic states in rubidium.

3.2.2 LRRM Structure Near $7s$-$5d_{5/2}$ Difference Frequency

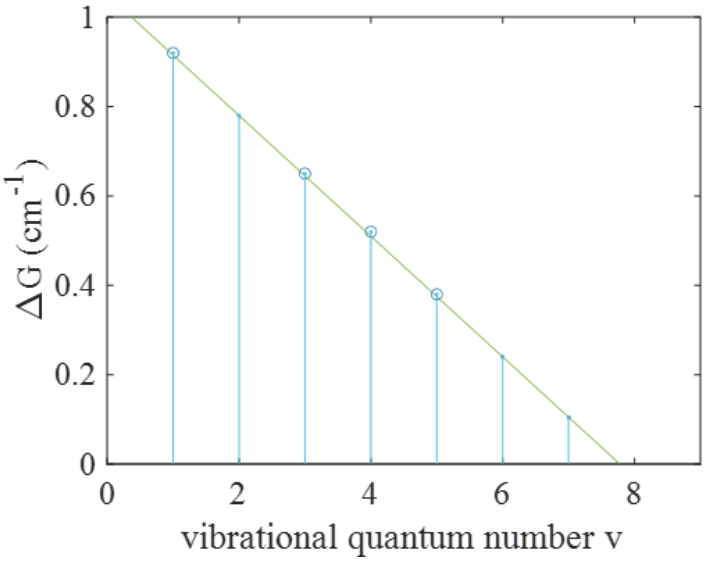

Figure 3.22: Equal energy spacing (fundamental frequency of overtones) ΔG as a function of the vibrational quantum number v (the vibrational quantum number) associated with the $7s$-$5d_{5/2}$ quantum beat. The relation was fitted with a linear function and additional vibrational energy spacing was deduced from the fitted function, which brings the total number of energy spacings between vibrational levels within the well to 7. The dissociation energy D_0 and D_e can be obtained by calculating the total area under the fitted curve. Open circle: Observed ΔG. Blue dots: Derived ΔG but not observed.

The long-range Rydberg molecular structures can also be observed on both sides of the $7s$-$5d_{5/2}$ quantum beating peak as vibrational equal energy spacing overtones, as shown in Figure 3.13. Five series of overtones are identified in Figure 3.13. The fundamental frequencies of the overtones ΔG are marked in the figure next to each series.

Let us for now ignore the largest energy spacing of 2.48 cm^{-1} as it does not fit into the same anharmonic oscillator model with other spacings. It may belong to another quantum well whose other vibrational energy spacings have not been identified. Similar to the $8s$-$6d_{5/2}$ case, each energy spacing of a series is assigned an integer number $v = 1, 2, 3$, etc. The energy spacing ΔG is plotted as a function of the vibrational quantum number v and is shown in Figure 3.22.

A linear relation is found between ΔG and v. Fitting the relation with

Equation 3.6 yields the vibrational constants for an electronic quantum well associated with the $7s$-$5d_{5/2}$ quantum beating

$$\begin{aligned} \omega_e &= 1.23 \text{ cm}^{-1} \\ \omega_e x_e &= 0.07 \text{ cm}^{-1} \end{aligned} \tag{3.18}$$

Additional vibrational energy spacings within the well can be derived and are marked as blue dots in Figure 3.22, which brings the total number of energy spacings between vibrational levels within the well to 7. The dissociation energy D_0 can be obtained by calculating the total area under the fitted curve along with $D_e = D_0 + G(v = 0)$

$$\begin{aligned} D_{0-7s5d} &= 3.60 \text{ cm}^{-1} \\ D_{e-7s5d} &= 4.19 \text{ cm}^{-1} \end{aligned} \tag{3.19}$$

Utilizing Equations 3.15 and 3.17, the PEC of the quantum well is derived using Morse potential and is plotted in Figure 3.23. A total number of 8 vibrational levels are supported within the well and the equilibrium internuclear distance is an approximate estimation according to the scaling law.

The binding energy derived from the $7s$-$5d_{5/2}$ quantum beat is also compared with the predicted values from the scaling law as shown in Figure 3.21.

Vibrational constants extracted from the quantum beating spectrum for both $7s$-$5d_{5/2}$ and $8s$-$6d_{5/2}$ are summarized in Table 3.3. All vibrational constants of the first order measured from the quantum beating spectrum are similar to that extracted from [6]. Notice that only the well 1 of $8s$-$6d_{5/2}$ has the third and fourth order terms ($\omega_e y_e$, $\omega_e z_e$) that are significant enough to be measured. Its $\omega_e y_e = 0.05$ cm^{-1} is only slightly larger than the "apparent" resolution limit of the quantum beating spectrum Δf = 0.0191 cm^{-1}. Since the $\omega_e x_e$ values of both $8s$-$6d_{5/2}$ well 2 and the $7s$-$5d_{5/2}$ well are at least 5 times smaller than the $\omega_e x_e$ of $8s$-$6d_{5/2}$ well 1, their third order vibrational constants $\omega_e y_e$ should be much smaller than the $\omega_e y_e$ of $8s$-$6d_{5/2}$ well 1, too small to be measured with the current resolution of the quantum beating spectrum. On the other hand, the measured value of $w_e z_e$ for $8s$-$6d_{5/2}$ well 1 is 6 times smaller than the apparent resolution of the spectrum. Its absolute value might not be trustworthy but according to our discussion

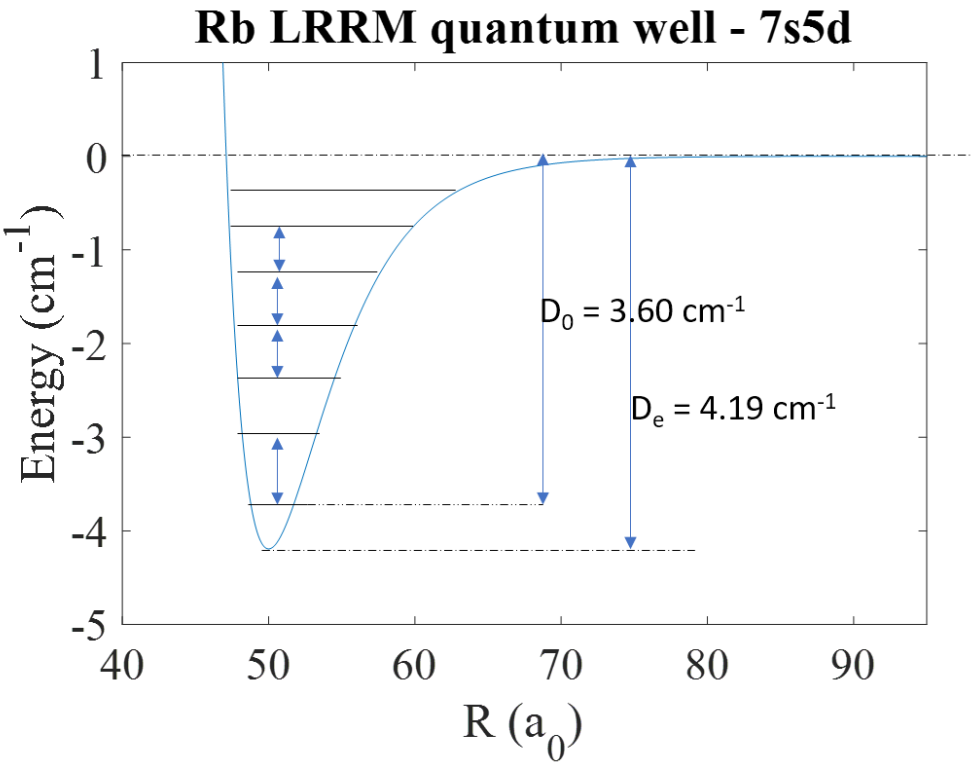

Figure 3.23: The derived potential energy curve for the LRRM associated with $7s$ and $5d$ atomic energy level asymptote. The potential curve is modeled as a Morse potential and the internuclear distance at equilibrium is chosen according to the scaling law. The dissociation energies of the wells are marked on the PEC. A number of supported vibrational energy levels are drawn within each well but their positions are only drawn approximately. The arrows designate the vibrational energy spacings that are observed on the quantum beat spectrum.

in Section 3.2.1, the existence of this term, albeit very small, is necessary to ensure limited-depth of the potential well.

Table 3.3: Vibrational constants extracted from the vibrational energy spacing overtones around $8s$-$6d_{5/2}$ and $7s$-$5d_{5/2}$ quantum beating signals. Notice that only the well 1 of $8s$-$6d_{5/2}$ has the third and fourth order terms that are significant enough to be measured.

	ω_e (cm^{-1})	$\omega_e x_e$ (cm^{-1})	$\omega_e y_e$ (cm^{-1})	$\omega_e z_e$ (cm^{-1})
$8s$-$6d_{5/2}$ well 1	3.19	0.51	0.05	-0.003
$8s$-$6d_{5/2}$ well 2	1.09	0.09		
$7s$-$5d_{5/2}$	1.23	0.07		
11p (C. H. Greene [6])	1.05			
7p (R. A. Carollo [29])	2			

These LRRMs we discovered in our experiments have very weak molecular bonds with binding energies less than 10 cm^{-1} (300 GHz), which is 2 orders of magnitude smaller than the thermal temperature (307 cm^{-1} or 9.21 THz at 170°C). We are able to observe the vibrational states within such shallow wells without preparing the samples at ultra-low temperature. The energy spacings between these vibrational levels manifest themselves as frequency overtones on both sides of their associated atomic level quantum beats on the quantum beat spectrum, which has a resolution high enough to resolve such vibrational energy spacing. The wide-bandwidth laser not only excites the Rydberg atomic energy levels but also photoassociates and excites the vibrational energy levels inside the quantum wells of these long-range Rydberg molecules. The wave packet becomes a superposition of both atomic wavefunctions and molecular wavefunctions. The wavefunctions associated with the atomic energy levels beat with the wavefunctions associated with the molecular vibrational energy levels and thus we see on the spectrum that the energy differences between the two classes of energy levels appear as quantum beat overtones on both sides of the much stronger atomic quantum beating peak.

Last but not least, a normalized nearest neighbor distribution of the rubidium gas vapor at 170° is shown in Figure 3.24. The calculation shows that out of the gas density of 2.5×10^{20} m^{-3}, 9×10^{-6} of the atoms have internuclear distances of 10-100 a_0, which are able to form the potential wells we observed.

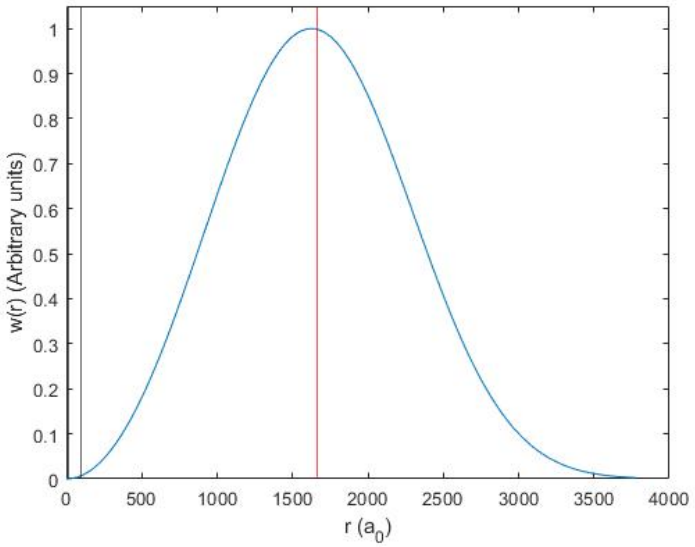

Figure 3.24: Nearest neighbor distribution of rubidium gas vapor at 170°. The y-axis is the relative number of the atoms at a given internuclear distance, with the maximum number normalized to be 1. X-axis is the internuclear distance in the units of Bohr radius (a_0). The mean internuclear distance is marked by the red vertical line and the range of internuclear distances that support LRRM's quantum wells are marked with black vertical lines (10-100 a_0). Out of the gas density of 2.5×10^{20} m^{-3}, 9×10^{-6} of the atoms have internuclear distances of 10-100 a_0.

3.2.3 Heteronuclear LRRM Structure on Quantum Beating Spectrum

Recall from Chapter 1 that long-range molecules are formed through the scattering process of a highly excited Rydberg electron off a ground state perturber. As the range of the polarization potential of the ground state perturber is much smaller than the Rydberg electron's de Broglie wavelength, the scattering process only serves to perturb the wavefunction of the Rydberg electron, causing phase shifts. Our discussions so far focused on the formation of LRRM in pure rubidium gas vapor, in which the only perturber is ground state rubidium. By including other atoms into the gas cell we are able to probe heteronuclear long-range Rydberg molecules with different composing perturber species. One example of such study is shown in Figure 3.25, where quantum beating spectrum at the vicinity of the $7s$-$5d_{5/2}$ atomic peaks is being compared from three different gas mixtures, **top:** rubidium gas vapor alone at 170 °C, **middle:** rubidium+cesium gas mixture

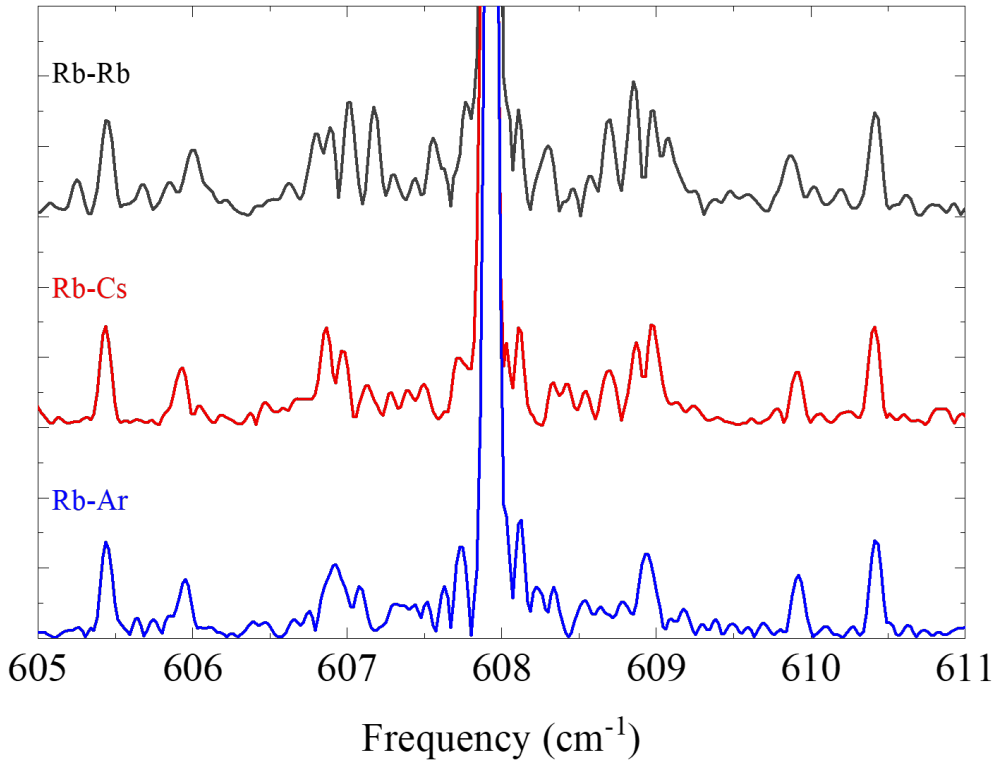

Figure 3.25: Comparison of the quantum beating spectra near the $7s$-$5d_{5/2}$ difference frequency for different sample species. Top: Rubidium gas vapor only. Middle: Rubidium and cesium gas mixture. Bottom: Rubidium and argon gas mixture. All other experimental conditions are the same.

at 170 °C and **bottom:** rubidium plus 1 Torr of Argon gas mixture at 170 °C. All the other experimental conditions are the same. Figure 3.25 shows that although the molecular structures look similar between the three sets of data, there are notable differences between them. There are disappearing/appearing and shifting of certain peaks. More investigations are needed to explain these differences in the quantum beating spectrum for different gas mixtures, particularly the difference in the scattering lengths of different ground state perturbers, which contributes to different potential energy curves and vibrational structures of the molecules. So far, Figure 3.25 proves that our quantum beating experimental is a promising experimental technique for the study of heteronuclear LRRM and the formation mechanism of LRRM.

CHAPTER 4

CONCLUSIONS

Quantum beat spectroscopy (QBS) is employed to study long-range Rydberg molecules (LRRM) for the first time. We are able to observe the weakly bound long-range Rydberg molecules (LRRMs) associated with rubidium atomic states with very low principal quantum numbers ($5d$, $6d$, $7s$ and $8s$). Energy spacings between adjacent vibrational levels within each LRRM's quantum well appear in frequency domain as overtones on both sides of the $7s$-$5d_{5/2}$ and $8s$-$6d_{5/2}$ atomic quantum beat peaks. We are able to extract vibrational constants for three potential wells and to calculate their dissociation energies and potential energy curves using Morse potential. Despite the fact that there are no direct results in the literature associated with S and D states at our principal quantum numbers, we are able to compare our vibrational constants with those of P state and extrapolate dissociation energies of our states using scaling law. These analyses show that our observations can be reasonably attributed to rubidium LRRM structure.

The study demonstrates a new experimental technique to study LRRM by using quantum beating experiment. This technique utilizes a high-power, ultrafast, wide-bandwidth laser source, in comparison to the more commonly used method of precision scanning of narrow-bandwidth lasers and field ionization. Instead of monitoring transitions between specifically targeted eigenstates in frequency domain, the quantum beating technique is able to probe non-stationary states composed of both atomic and molecular wavefunctions, resulting in a "wider-target" quantum beat spectrum using data obtained from time domain.

The technique also shows potential in studying heteronuclear LRRM, in particular, investigating the role of different ground-state perturbers in the electron-atom scattering process. Future work can further investigate the changes in quantum beating spectrum with different mixtures of alkali atoms and rare gas, at different temperature and pressure.

In addition, vibrational energy structures of LRRM can be analyzed to obtain electron-atom scattering lengths of various species, which are very difficult to measure experimentally. References [54] and [30] show examples of such work.

Because the experiments can be conducted with GHz resolution at heated gas temperature without preparing Bose-Einstein condensates, the quantum beating technique can be easily applied to the study of alkali-rare gas heteronuclear molecules (such as Rb-Ar). As it is relatively easy to prepare atomic ensemble at high temperature, the quantum beat technique may also find applications in studying long-range polyatomic molecules.

For long-range Rb_2, our experimental setup does not have resolution high enough to differentiate rubidium isotopes on the quantum beat spectrum. This limitation in resolution is purely instrumental, and is mainly due to the travel range and positioning errors of the translation stage for varying the pump-probe delay. Improving the linear stage, both in the maximum travel range and position accuracy, can further improve the resolution of the quantum beat spectrum, possibly revealing the isotope effects and hyperfine structures, even rotational structures.

On the theoretical side, it would be beneficial to compare the PEC derived from experimental data to theoretical computations. This involves solving PEC at low principal quantum numbers, where the Fermi pseudopotential becomes less accurate. The theoretical framework of LRRM remains to be improved in order to more accurately describe the molecular structure at low principal quantum numbers and the vibrational energy levels within each potential well. If more accurate theoretical description of the potential curves can be obtained, more accurate modeling of the potential curves from the experimental data other than the Morse potential can also be employed to better compare experimental data with theory.

REFERENCES

[1] C. H. Greene, A. S. Dickinson, and H. R. Sadeghpour, "Creation of polar and nonpolar ultra-long-range Rydberg molecules," *Physical Review Letters*, vol. 85, no. 12, pp. 2458–2461, 2000.

[2] E. Fermi, "Sopra lo spostamento per pressione delle righe elevate delle serie spettrali," *Nuovo Cimento*, vol. 11, p. 157, 1934.

[3] A. Omont, "On the theory of collisions of atoms in Rydberg states with neutral particles," *Journal de Physique*, vol. 38, no. 11, pp. 1343–1359, 1977.

[4] E. L. Hamilton, C. H. Greene, and H. R. Sadeghpour, "Shape-resonance-induced long-range molecular Rydberg states," *Journal of Physics B: Atomic, Molecular and Optical Physics*, vol. 35, no. 10, 2002.

[5] M. I. Chibisov, A. A. Khuskivadze, and I. I. Fabrikant, "Energies and dipole moments of long-range molecular Rydberg states," *Journal of Physics B: Atomic, Molecular and Optical Physics*, vol. 35, no. 10, pp. L193–L198, 2002.

[6] C. H. Greene, E. L. Hamilton, H. Crowell, C. Vadla, and K. Niemax, "Experimental verification of minima in excited long-range Rydberg states of Rb_2," *Physical Review Letters*, vol. 97, no. 23, pp. 8–11, 2006.

[7] C. Vadla, V. Horvatic, and K. Niemax, "Line-broadening studies of excited diatomic homoatomic and heteroatomic Rydberg molecules formed by potassium, rubidium, and cesium atoms," *Physical Review A*, vol. 80, no. 5, p. 052506, 2009.

[8] V. Bendkowsky, B. Butscher, J. Nipper, J. P. Shaffer, R. Löw, and T. Pfau, "Observation of ultralong-range Rydberg molecules," *Nature*, vol. 458, no. 7241, pp. 1005–1008, 2009.

[9] T. Niederprüm, O. Thomas, T. Eichert, and H. Ott, "Rydberg molecule-induced remote spin flips," *Physical Review Letters*, vol. 117, no. 12, p. 123002, 2016.

[10] T. Niederprüm, O. Thomas, T. Eichert, C. Lippe, J. Pérez-Ríos, C. H. Greene, and H. Ott, "Observation of pendular butterfly Rydberg molecules," *Nature Communications*, vol. 7, no. 1, pp. 1–6, 2016.

[11] M. Bellos, R. Carollo, J. Banerjee, E. Eyler, P. Gould, and W. Stwalley, "Excitation of weakly bound molecules to trilobitelike Rydberg states," *Physical review letters*, vol. 111, no. 5, p. 053001, 2013.

[12] D. Booth, S. Rittenhouse, J. Yang, H. Sadeghpour, and J. Shaffer, "Production of trilobite Rydberg molecule dimers with kilo-Debye permanent electric dipole moments," *Science*, vol. 348, no. 6230, pp. 99–102, 2015.

[13] A. T. Krupp, "D-state Rydberg electrons interacting with ultracold atoms," Ph.D. dissertation, University of Stuttgart, 2014.

[14] D. A. Anderson, S. A. Miller, and G. Raithel, "Photoassociation of long-range nD Rydberg molecules," *Physical Review Letters*, vol. 112, no. 16, pp. 1–5, 2014.

[15] J. Tallant, S. Rittenhouse, D. Booth, H. Sadeghpour, and J. Shaffer, "Observation of blueshifted ultralong-range Cs_2 Rydberg molecules," *Physical review letters*, vol. 109, no. 17, p. 173202, 2012.

[16] W. Demtröder, *Laser Spectroscopy: Vol. 2: Experimental Techniques*. Springer Science & Business Media, 2008, vol. 2.

[17] J. Shaffer, S. Rittenhouse, and H. Sadeghpour, "Ultracold Rydberg molecules," *Nature Communications*, vol. 9, no. 1, pp. 1–12, 2018.

[18] C. Fey, F. Hummel, and P. Schmelcher, "Ultralong-range Rydberg molecules," *Molecular Physics*, vol. 118, no. 2, p. e1679401, 2020.

[19] M. T. Eiles, "Trilobites, butterflies, and other exotic specimens of long-range Rydberg molecules," *Journal of Physics B: Atomic, Molecular and Optical Physics*, vol. 52, no. 11, 2019.

[20] T. F. Gallagher, *Rydberg Atoms*. Cambridge University Press, 1994.

[21] N. Bohr, "On the constitution of atoms and molecules," *The London, Edinburgh, and Dublin Philosophical Magazine and Journal of Science*, vol. 26, no. 153, pp. 476–502, 1913.

[22] N. Bohr, "Über die serienspektra der elemente," *Zeitschrift für Physik A Hadrons and Nuclei*, vol. 2, no. 5, pp. 423–469, 1920.

[23] J. R. Rydberg, "On the structure of the line-spectra of the chemical elements," *The London, Edinburgh, and Dublin Philosophical Magazine and Journal of Science*, vol. 29, no. 179, pp. 331–337, 1890.

[24] W. Ritz, "Magnetische atomfelder und serienspektren," *Annalen der Physik*, vol. 330, no. 4, pp. 660–696, 1908.

[25] C. H. Greene and M. Aymar, "Spin-orbit effects in the heavy alkaline-earth atoms," *Phys. Rev. A*, vol. 44, pp. 1773–1790, Aug 1991.

[26] W. Li, I. Mourachko, M. W. Noel, and T. F. Gallagher, "Millimeter-wave spectroscopy of cold Rb Rydberg atoms in a magneto-optical trap: Quantum defects of the ns, np, and nd series," *Phys. Rev. A*, vol. 67, p. 052502, May 2003.

[27] J. Han, Y. Jamil, D. V. L. Norum, P. J. Tanner, and T. F. Gallagher, "Rb nf quantum defects from millimeter-wave spectroscopy of cold ^{85}Rb Rydberg atoms," *Phys. Rev. A*, vol. 74, p. 054502, Nov 2006.

[28] M. T. Eiles and C. H. Greene, "Hamiltonian for the inclusion of spin effects in long-range Rydberg molecules," *Phys. Rev. A*, vol. 95, p. 042515, Apr 2017.

[29] R. A. Carollo, J. L. Carini, E. E. Eyler, P. L. Gould, and W. C. Stwalley, "High-resolution spectroscopy of Rydberg molecular states of Rb_2 85 near the $5s$+$7p$ asymptote," *Physical Review A*, vol. 95, no. 4, pp. 1–8, 2017.

[30] J. L. MacLennan, Y.-J. Chen, and G. Raithel, "Deeply bound (24 d j+ 5 s 1/2) Rb 87 and Rb 85 molecules for eight spin couplings," *Physical Review A*, vol. 99, no. 3, p. 033407, 2019.

[31] E. Schrödinger, *Collected Papers on Wave Mechanics*. London and Glasgow, 1929.

[32] H. Bitto and J. R. Huber, "Molecular quantum beat spectroscopy," *Optics Communications*, vol. 80, no. 2, pp. 184–198, 1990.

[33] S. Haroche, "Quantum beats and time-resolved fluorescence spectroscopy," in *High-resolution Laser Spectroscopy*. Springer, 1976, pp. 253–313.

[34] W. Gornik, D. Kaiser, W. Lange, J. Luther, and H.-H. Schulz, "Quantum beats under pulsed dye laser excitation," *Optics Communications*, vol. 6, no. 4, pp. 327–328, 1972.

[35] S. Haroche, M. Gross, and M. Silverman, "Observation of fine-structure quantum beats following stepwise excitation in sodium d states," *Physical Review Letters*, vol. 33, no. 18, p. 1063, 1974.

[36] G. Alber, H. Ritsch, and P. Zoller, "Generation and detection of Rydberg wave packets by short laser pulses," *Physical Review A*, vol. 34, no. 2, p. 1058, 1986.

[37] H. Tran, P. John, and J. Eden, "Quantum beating among the s, p, and d orbitals of atomic Rb," in *Quantum Electronics and Laser Science Conference*. Optical Society of America, 1995, p. QThG34.

[38] H. Tran, P. John, J. Gao, and J. G. Eden, "Interaction of atomic wave packets with four-wave mixing: Detection of rubidium and potassium wave packets by coherent ultraviolet emission," *Optics Letters*, vol. 23, no. 1, pp. 70–72, 1998.

[39] A. L. Oldenburg, "Dynamics of electronic wavepackets in atomic Rubidium," Ph.D. dissertation, University of Illinois at Urbana-Champaign, 2002.

[40] T. M. Spinka, "Nonlinear optical processes and the nearest neighbor distribution in rubidium vapor," Ph.D. dissertation, University of Illinois at Urbana-Champaign, 2010.

[41] B. Ricconi, "Quantum beat observations in rubidium vapor," Ph.D. dissertation, University of Illinois at Urbana-Champaign, 2012.

[42] A. Senin, H. Tran, J. Gao, Z. Lu, C. Zhu, A. Oldenburg, J. Allen, and J. G. Eden, "Molecular dissociation observed with an atomic wavepacket and parametric four-wave mixing," *Chemical Physics Letters*, vol. 381, no. 1-2, pp. 53–59, 2003.

[43] A. A. Senin, "Study of wavepacket dynamics in rubidium vapor by means of time-frequency analysis." Ph.D. dissertation, University of Illinois at Urbana-Champaign, 2004.

[44] Y. Xiao, A. Senin, B. Ricconi, R. Kogler, C. Zhu, and J. G. Eden, "Molecular dissociation and nascent product state distributions detected with atomic wavepacket interferometry and parametric four-wave mixing: Rb_2 predissociation observed by quantum beating in Rb at 18.2 THz," *Journal of Physics B: Atomic, Molecular and Optical Physics*, vol. 41, no. 18, p. 185101, 2008.

[45] Y. Xiao, "Probing the dissociation of the rubidium dimer by wavepackets and parametric four-wave mixing," Ph.D. dissertation, University of Illinois at Urbana-Champaign, 2007.

[46] W. Goldshlag, "Dynamics of interfering wave packets in rubidium by high resolution quantum beat spectroscopy," Ph.D. dissertation, University of Illinois at Urbana-Champaign, 2017.

[47] C. E. Shannon, "Communication in the presence of noise," *Proceedings of the IRE*, vol. 37, no. 1, pp. 10–21, Jan 1949.

[48] A. V. Oppenheim and R. W. Schafer, *Discrete-Time Signal Processing*, 3rd ed. USA: Prentice Hall Press, 2009.

[49] R. G. Lyons, *Understanding Digital Signal Processing, 3/E.* Pearson Education India, 2004.

[50] I. Blagouchine and E. Moreau, "Analytic method for the computation of the total harmonic distortion by the Cauchy method of residues," *Communications, IEEE Transactions on*, vol. 59, pp. 2478–2491, 09 2011.

[51] B. Broers, H. van den Heuvell, van Linden, and L. Noordam, "Efficient population transfer in a three-level ladder system by frequency-swept ultrashort laser pulses," *Physical Review Letters*, vol. 69, no. 14, p. 2062, 1992.

[52] G. Herzberg, *Molecular Spectra and Molecular Structure.* Van Nostrand, 1957.

[53] P. M. Morse, "Diatomic molecules according to the wave mechanics. ii. vibrational levels," *Phys. Rev.*, vol. 34, pp. 57–64, Jul 1929.

[54] H. Saßmannshausen, J. Deiglmayr, and F. Merkt, "Long-range Rydberg molecules, Rydberg macrodimers and Rydberg aggregates in an ultracold Cs gas," *The European Physical Journal Special Topics*, vol. 225, no. 15, pp. 2891–2918, 2016.